International Journal of Nanomedicine

Dovepress
Taylor & Francis Group

Open Access Full Text Article

ORIGINAL RESEARCH

Macrophage-Derived CuET Vesicles Synergistically Enhance Paclitaxel Efficacy by Inhibiting Tumor Growth and Boosting Immunity in Breast Cancer

Xiaoling Guo[1,*], Lina Zhou[2,3,*], Anya Buerliesi[1,*], Jiahui Ye[1], Yinhua Lv[1,3], Wenqian Wei[1,3], Jinlan Jiao[1], Weihong Ge[2–4], Yun Zhu[2–4], Weijie Zhang[1,3]

[1]Division of Breast Surgery, Department of General Surgery, Nanjing Drum Tower Hospital, The Affiliated Hospital of Medical School, Nanjing University, Nanjing, 210008, People's Republic of China; [2]Department of Pharmacy, Nanjing Drum Tower Hospital Clinical College of Nanjing University of Chinese Medicine, Nanjing, 210008, People's Republic of China; [3]Department of Pharmacy, Nanjing Drum Tower Hospital, Drum Tower Clinical Medical College of Nanjing Medical University, Nanjing, 210000, People's Republic of China; [4]Nanjing Medical Center for Clinical Pharmacy, Nanjing, 210008, People's Republic of China

*These authors contributed equally to this work

Correspondence: Yun Zhu; Weijie Zhang, Email njglyyzhuy@cpu.edu.cn; zhangweijie1616@nju.edu.cn

Background: Paclitaxel is a cornerstone of breast cancer treatment, but its efficacy is often limited by low response rates and drug resistance. To address this, we developed MEVs@CuET, a novel therapeutic approach combining cuproptosis-inducing copper(II) complex (CuET) with macrophage-derived extracellular vesicles (MEVs), aiming to enhance paclitaxel's antitumor effects.

Methods: The tumor-targeting capability of MEVs@CuET was evaluated through cellular uptake and in vivo distribution studies. In vitro synergy was assessed using the ZIP model, while transcriptome sequencing analyzed gene expression changes. In vivo antitumor activity and immune modulation were examined in breast cancer models, with tumor growth inhibition, apoptosis, and Th17 lymphocyte levels measured.

Results: MEVs@CuET demonstrated efficient tumor targeting and synergistic antiproliferative effects with paclitaxel in vitro (synergy score: 29.37). Transcriptomic analysis revealed significant alterations in immune-related pathways, particularly upregulation of the IL-17 signaling pathway. In vivo, the combination therapy markedly inhibited tumor growth, increased apoptosis, and elevated Th17 cell levels, aligning with the transcriptomic findings.

Conclusion: MEVs@CuET significantly enhances paclitaxel's efficacy by inducing cuproptosis and modulating antitumor immunity, offering a promising strategy to overcome resistance in breast cancer treatment.

Keywords: breast cancer, Paclitaxel, macrophage-derived extracellular vesicles, cuproptosis, combination therapy

Introduction

Breast cancer remains one of the most frequently diagnosed malignancies among women worldwide, with high morbidity and mortality rates.[1–3] Despite advances in targeted therapies and immunotherapy-such as HER2-targeted agents and immune checkpoint inhibitors-chemotherapy continues to serve as a cornerstone of treatment, especially for patients with advanced or triple-negative disease. Among chemotherapeutic agents, paclitaxel plays a central role due to its microtubule-stabilizing properties, which induce G2/M phase cell cycle arrest and promote apoptosis.[4,5] However, its clinical utility is often limited by the development of drug resistance and dose-limiting toxicities, including neurotoxicity and myelosuppression.[6–8] This challenge is particularly prominent in triple-negative breast cancer, an aggressive subtype that lacks effective therapeutic targets, relies heavily on paclitaxel, yet frequently encounters resistance with limited targeted options available.[9,10] This unmet clinical need underscores the urgency for developing novel combination strategies that can enhance the sensitivity and efficacy of paclitaxel.

https://doi.org/10.2147/IJN.S570540
Received: 16 October 2025
Accepted: 6 February 2026
Published: 16 February 2026

One promising approach involves leveraging novel forms of regulated cell death to sensitize tumor cells to conventional chemotherapeutics. Cuproptosis, a recently identified copper-dependent form of cell death, has attracted increasing attention in cancer research.[11–13] This mechanism relies on the accumulation of intracellular copper ions, which bind to lipoylated proteins in the tricarboxylic acid (TCA) cycle, leading to protein aggregation, mitochondrial dysfunction, and proteotoxic stress.[14] Given that many cancer cells, particularly those rich in mitochondria, are highly sensitive to oxidative and proteotoxic stress, cuproptosis represents a potentially selective and effective anti-tumor strategy.[15–17] Immunogenic cell death (ICD), such as that induced by certain chemotherapeutic agents or metal-based compounds,[18] can stimulate the release of damage-associated molecular patterns (DAMPs), which activate dendritic cells and initiate adaptive immune responses.[19–23] Notably, emerging evidence suggests that cuproptosis, beyond its direct cytotoxic effects, can function as a potent trigger of immunogenic cell death (ICD).[24] The process is associated with the exposure of calreticulin (CRT) and the release of high-mobility group box 1 (HMGB1), which are crucial DAMPs for dendritic cell maturation and subsequent T cell activation.[25] This link provides a strong mechanistic foundation for the potential of cuproptosis inducers like CuET to not only kill tumor cells but also to stimulate an adaptive anti-tumor immune response. Thus, combining cuproptosis with paclitaxel could synergistically inhibit tumor growth through both direct cytotoxic effects and immune activation. However, achieving sufficient intracellular copper concentrations without inducing systemic toxicity remains a major barrier to its clinical application. Therefore, developing safe and efficient delivery systems capable of targeting copper-based compounds specifically to tumor cells is essential.

To address this challenge, recent advances in nanotechnology have led to the development of biomimetic drug delivery platforms, particularly extracellular vesicles (EVs), which offer unique advantages over synthetic nanoparticles.[26] EVs derived from macrophages (MEVs) are especially promising due to their intrinsic biocompatibility, prolonged circulation time, and natural ability to target inflammatory and tumor sites.[27–29] Macrophages play a central role in immune surveillance and inflammation, and their secreted vesicles retain key surface receptors and signaling molecules that facilitate tumor homing and immune evasion.[30–34] Additionally, MEVs are less likely to trigger immune clearance compared to synthetic carriers,[35–39] making them ideal candidates for targeted therapy. By engineering MEVs to carry cuproptosis-inducing agents, it may be possible to achieve localized and sustained tumor cell death while minimizing off-target effects.

In light of these considerations, we designed a therapeutic strategy based on macrophage-derived extracellular vesicles loaded with CuET (MEVs@CuET), a small-molecule cuproptosis inducer, which could selectively deliver CuET to breast cancer cells, elevate intracellular copper levels, and thereby induce cuproptosis. To investigate its potential to enhance chemosensitivity, MEVs@CuET was combined with paclitaxel to evaluate the synergistic antitumor effect, as illustrated in Scheme 1. The synergistic efficacy of MEVs@CuET and paclitaxel was first verified in vitro using breast cancer cell lines, followed by evaluation of key cuproptosis-related signaling pathways to confirm the mechanism of action. RNA-Seq technology was subsequently used to screen for differentially expressed genes and signaling pathways potentially involved in enhancing tumor cell sensitivity to chemotherapy. Finally, the in situ distribution of MEVs@CuET in 4T1 tumor-bearing mouse models was investigated, and its antitumor efficacy, along with immune activation effects, was validated in vivo. This study aimed to inspire new strategies for improving the responsiveness of resistant breast cancers to conventional chemotherapeutic agents through targeted induction of cuproptosis.

Materials and Methods

Materials Preparation

Unless otherwise stated, all chemicals were purchased from commercial suppliers (Beyotime Biotechnology and Thermo Fisher Scientific) and used without further purification. CCK-8 reagent was obtained from DOJINDO LABORATORIES. The Annexin V-FITC/PI Apoptosis Detection Kit and Cell Cycle and Apoptosis Analysis Kit were purchased from Vazyme. Hoechst 33,342 was acquired from KeyGEN BioTECH (Nanjing, China). Rabbit anti-CD14 (F1070) was sourced from Selleck, and mouse anti-GAPDH (60004-1-IG) was obtained from Proteintech. Goat anti-rabbit IgG (H&L)-HRP and goat anti-mouse IgG (H&L)-HRP were purchased from Bioworld Technology Co. CD3, CD4, CD45, and IL-17A flow cytometry antibodies were acquired from BD Biosciences. Paclitaxel was sourced from Selleck, and

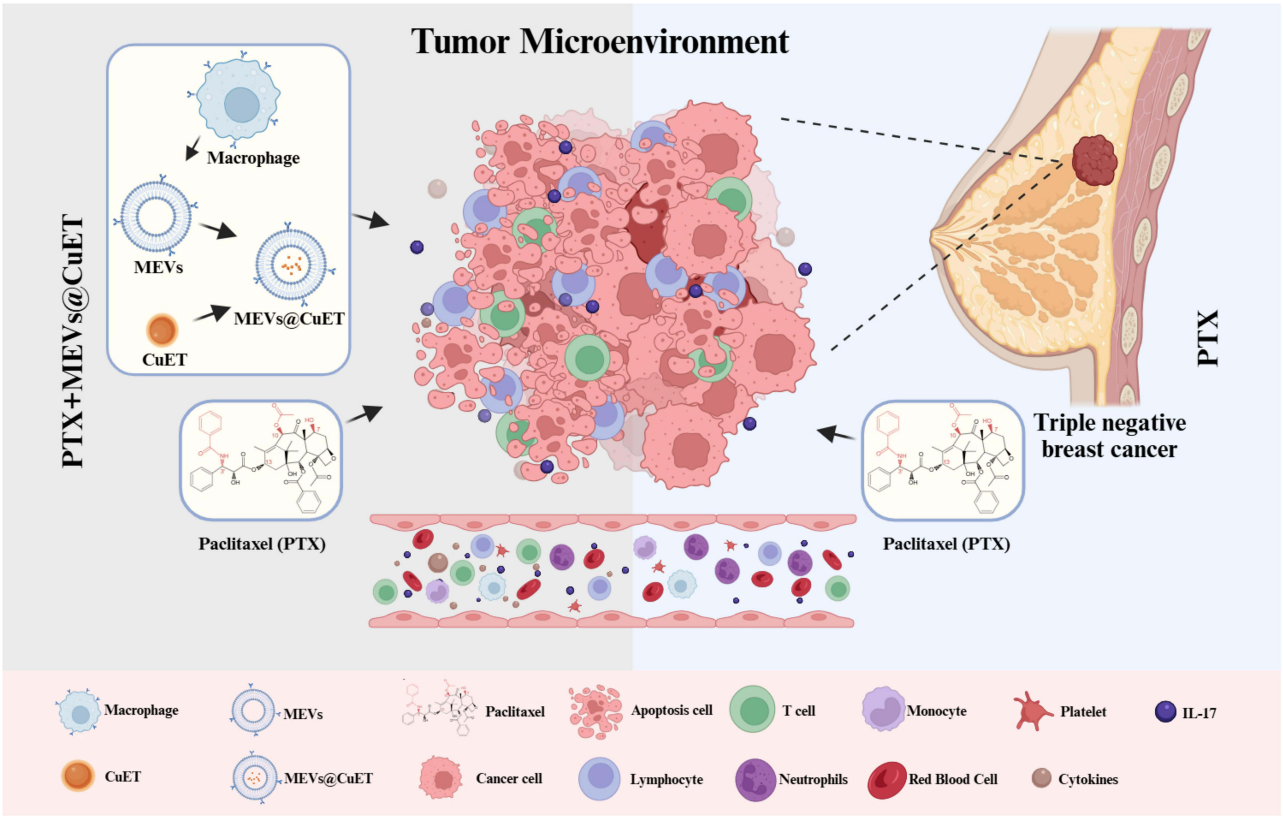

Scheme 1 Schematic illustration of the synergistic therapeutic enhancement of paclitaxel against triple-negative breast cancer through MEVs@CuET combination therapy.

bis(diethyldithiocarbamate)copper (CuET) was purchased from Shanghai Aladdin Biochemical Technology Co., Ltd. Isoflurane was obtained from Qingdao Oubang Pharmaceutical Technology Co., Ltd. (Batch No.: 20220905). Trypsin, phosphate-buffered saline (PBS), fetal bovine serum (FBS), and DMEM were obtained from SenBeijia Biological Technology Co. Deionized water (18.2 MΩ cm) from a Milli-Q purification system was used for all preparations.

Cell Lines

The mouse breast cancer cell line (4T1) and mouse embryonic fibroblast cell line (NIH/3T3) used in this study were obtained from the Cell Bank of the Shanghai Institute of Biochemistry and Cell Biology, Chinese Academy of Sciences. Cells were cultured in DMEM/F-12 medium supplemented with 10% (v/v) FBS, 100 U/mL penicillin, and 100 μg/mL streptomycin at 37 °C in a humidified incubator with 5% CO_2. Cells were passaged and experiments were conducted during the exponential growth phase or at cell densities mentioned in the literature.

The mouse monocyte-macrophage cell line (RAW264.7) was purchased from the Kunming Cell Bank of the Chinese Academy of Sciences and cultured in high-glucose DMEM supplemented with 10% FBS and 1% penicillin-streptomycin at 37 °C with 5% CO_2. To effectively collect RAW264.7-derived extracellular vesicles, FBS was centrifuged at 55,000 rpm for 120 minutes to remove vesicles, and the entire process was performed under sterile conditions.

Extraction of Macrophage and Red Blood Cell Membranes

Macrophage membranes were extracted from RAW264.7 cells using a freeze-thaw method. RAW264.7 cells were expanded in high-glucose DMEM, centrifuged at 600 × g for 5 minutes at 4 °C, and the cell pellet was resuspended in membrane protein extraction reagent containing PMSF. After incubation on ice for over 30 minutes, the cells were subjected to repeated freeze-thaw cycles (liquid nitrogen and 30 °C) 6–7 times. The lysate was centrifuged at 700 × g for 10 minutes at 4 °C to remove organelles, followed by centrifugation at 14,000 × g for 30 minutes at 4 °C to obtain the

https://doi.org/10.2147/IJN.S570540

membrane pellet. The pellet was resuspended in 50–100 μL PBS, and the macrophage membrane (MCM) suspension was stored at −80 °C after BCA protein quantification.

Red blood cell membranes were extracted using a hypotonic method. Mouse whole blood (3 mL) was centrifuged at 3,000 rpm for 5 minutes, and the plasma, white blood cells, and platelets were discarded. The pellet was washed with 1× PBS until the supernatant was colorless (typically 3 washes). The pellet was resuspended in 0.25× PBS (1:50 ratio) and incubated overnight at 4 °C for hypotonic lysis. The lysate was centrifuged at 8,000 rpm for 15 minutes at 4 °C, and the pellet was washed with 0.25× PBS to obtain a pale pink cell mass. The red blood cell membrane pellet was resuspended in an equal volume of PBS (100–200 μL) and stored at −80 °C after BCA protein quantification.

Preparation and Characterization of Macrophage-Derived Extracellular Vesicles

The extracted macrophage membranes were sonicated on ice using a low-power ultrasonic probe to form MEVs. Equal protein concentrations of MCM and MEVs were separated by 10% SDS-PAGE. One portion of the samples was stained with Coomassie Brilliant Blue, while another portion was transferred to a PVDF membrane. The membrane was pre-incubated in TBS buffer containing 5% skim milk and 0.05% Tween 20 for 2 hours, followed by overnight hybridization with CD14 primary antibody at 4 °C. The membrane was then incubated with an appropriate horseradish peroxidase (HRP)-conjugated secondary antibody for 2 hours. Protein bands were detected using an enhanced chemiluminescence detection kit.

Preparation of MEVs@CuET and REVs@CuET

CuET (1 mg) was dissolved in 10 mL of pure water. The extracted macrophage membranes and red blood cell membranes were mixed with the drug solution in equal volumes, sonicated on ice using a 26 W ultrasonic probe (3 s on, 5 s off for 30s), and extruded through a 600 nm polycarbonate membrane 25 times, followed by extrusion through a 400 nm polycarbonate membrane 25 times. The mixture was centrifuged at 830 rpm for 15 minutes and then at 3,000 rpm for 10 minutes at room temperature. The supernatant containing the biomimetic nanoparticles was stored at 4 °C. A standard curve for CuET was generated using a Nanodrop spectrophotometer by measuring the absorbance at 290 nm. The absorbance of MEVs@CuET was measured and substituted into the standard curve equation to determine the CuET concentration.

The encapsulation efficiency (EE) and drug loading capacity (DLC) were calculated using the following equations:

EE (%) = (Amount of CuET in purified MEVs@CuET/Total amount of CuET used in formulation) × 100

DLC (%) = (Weight of CuET in MEVs@CuET/Total weight of MEVs@CuET) × 100

Preparation of MEVs@DiI and REVs@DiI

DiI (2 mg) was dissolved in 1 mL of ethanol and mixed with the membrane solution at a 1:10 ratio. The mixture was sonicated on ice and extruded through 600 nm and 400 nm polycarbonate membranes 25 times each. The final DiI concentration in the preparation was 100 μg/mL, as measured using a Spark™ 10 μm multimode microplate reader (Tecan Group Ltd., Männedorf, Switzerland).

Preparation of MEVs@CuET/IR 780 and REVs@CuET/IR 780

IR 780 (2 mg) was dissolved in 1 mL of ethanol and mixed with the membrane solution in equal volumes. The mixture was sonicated on ice and extruded through 600 nm and 400 nm polycarbonate membranes 25 times each. The preparation was centrifuged at 830 rpm for 15 minutes and then at 3,000 rpm for 10 minutes at room temperature in the dark. The supernatant was collected and stored.

Cell Viability Assay (CCK-8 Method)

The effects of MEVs@CuET and REVs@CuET on 4T1 and NIH/3T3 cell proliferation were assessed using the CCK-8 assay. Cells were seeded in 96-well plates at 5×10^3 cells/well and treated with MEVs@CuET (0.1–1.0 μg/mL or 1.0–32.0 μg/mL) or REVs@CuET (0.1–1.0 μg/mL) for 24 and 48 hours. After treatment, 10 μL of CCK-8 solution was added to each well, and the plates were incubated for 4 hours. Absorbance was measured at 450 nm using an ELISA

microplate reader (Spectra Max 190, Molecular Devices, USA). Cell viability was calculated as (experimental group absorbance – blank absorbance)/(control group absorbance – blank absorbance) × 100%.

Drug Synergy Calculation

The synergistic effects of paclitaxel and MEVs@CuET were evaluated using the CCK-8 assay. The cell inhibition rate was calculated as (control group absorbance – experimental group absorbance)/(control group absorbance – blank absorbance) × 100%. The data were imported into SynergyFinder (https://synergyfinder.fimm.fi) in the required format (drug concentration vs cell survival/inhibition rate matrix). The ZIP model was selected, and parameters such as drug names and concentration units were input to calculate synergy scores, generate heatmaps, 3D plots, and dose-response curves.

Cellular Uptake Assay

The uptake of MEVs@DiI and REVs@DiI by 4T1 cells was assessed using fluorescence microscopy. Cells were seeded in confocal dishes and cultured for 24 hours. After incubation with MEVs@DiI or REVs@DiI for 2, 4, and 6 hours, cells were washed with PBS, fixed with 4% paraformaldehyde for 10 minutes, and stained with DAPI for 10 minutes. Cells were preserved in phosphate buffer and observed under a fluorescence microscope (Leica THUNDER Imager Live Cell). Each experiment was performed in triplicate.

Live/Dead Cell Staining and Flow Cytometry Analysis

Cells were seeded in 12-well plates and cultured for 24 hours. After treatment with paclitaxel, MEVs@CuET, or the combination, cells were stained with calcein-AM/PI (Beyotime Biotechnology) and observed under a fluorescence microscope (Leica THUNDER Imager Live Cell). For flow cytometry, cells were seeded in 6-well plates and treated as described above. Floating and adherent cells were collected, stained with calcein-AM/PI, and analyzed using a FACSCalibur flow cytometer (Becton Dickinson, Franklin Lakes, USA). Data were analyzed using FlowJo V10 software and expressed as mean ± SD (n = 3).

Apoptosis Analysis by Flow Cytometry

Apoptosis was assessed using the Annexin V-FITC/PI Kit. Cells were treated as described, collected, and stained with Annexin V-FITC/PI. After 30 minutes of incubation, cells were analyzed using a FACSCalibur flow cytometer. Data were analyzed using FlowJo V10 software and expressed as mean ± SD (n = 3).

RNA Sample Preparation and Library Construction for Sequencing

Total RNA was extracted from 4T1 cells using TRIZOL after treatment with paclitaxel, MEVs@CuET, or the combination. RNA concentration, purity (A260/A280 ratio: 1.8–2.1), and integrity (RIN > 8.0) were assessed using a Nanodrop spectrophotometer and Agilent Bioanalyzer. RNA libraries were constructed using the Illumina TruSeq RNA Library Prep Kit and sequenced on an Illumina NovaSeq 6000 (paired-end, PE150).

Transcriptome Sequencing Data Analysis

Raw sequencing data were processed using fastp (https://github.com/OpenGene/fastp) to remove adapter sequences, low-quality bases, and reads with >10% N content. Clean data were subjected to quality assessment, including base error rate and content distribution analysis.

Clean reads were aligned to the reference genome using HISAT2 (http://ccb.jhu.edu/software/hisat2/index.shtml). Alignment quality was assessed based on sequencing saturation, gene coverage, and read distribution across genomic regions and chromosomes.

Gene and transcript expression levels were quantified using RSEM (http://deweylab.github.io/RSEM/). Read counts were used for subsequent differential expression analysis.

Differentially expressed genes (DEGs) were identified using DEGseq (https://www.rdocumentation.org/packages/DEGseq/versions/1.26.0). Genes with FDR < 0.05 and $|\log2FC| \geq 1$ were considered DEGs.

DEGs were annotated and enriched using GO (http://geneontology.org/), KEGG (https://www.genome.jp/kegg/), and Reactome (https://reactome.org) databases. Enrichment analysis was performed using Goatools (https://github.com/tanghaibao/GOatools), Python scipy (https://scipy.org/install/), and Reactome's hypergeometric test.

Vitro Assays for IL-17 and Th17 Cell

Spleens were harvested from euthanized mice, homogenized in PBS, filtered through a 70 μm cell strainer, and treated with ACK lysis buffer to remove red blood cells. Lymphocytes were resuspended in complete medium.

Splenic lymphocytes were stained with CD3, CD4, CD45, and IL-17A antibodies, fixed, permeabilized, and analyzed using a CytoFLEX S flow cytometer (Beckman). Data were analyzed using FlowJo V10 software.IL-17 levels in serum and cell culture supernatants were measured using a mouse IL-17 ELISA kit (Jiangsu Enzyme Immunoassay). Absorbance was measured at 450 nm using a microplate reader (Spectra Max 190, Molecular Devices, USA).

Biodistribution Analysis

MEVs@CuET/IR 780 and REVs@CuET/IR 780 were injected into 4T1 tumor-bearing mice via the tail vein. In vivo NIR imaging was performed at 2, 4, 8, 12, and 24 hours post-injection using a Calper IVIS Lumina II imaging system. Fluorescence intensity in tumors and organs was quantified.

Vivo Antitumor Assays

For the in vivo efficacy study, tumor-bearing mice were randomly assigned to the different treatment groups. The investigator responsible for tumor volume measurements and endpoint tissue collection was blinded to the group allocation to minimize bias.

Six- to eight-week-old female BALB/c mice were obtained from Jiangsu GemPharmatech Co., Ltd. (Nanjing, China) and housed under specific pathogen-free (SPF) conditions in a controlled environment with a 12-hour light/dark cycle (lights on at 7:00 AM), a constant temperature of 22 ± 2°C, and relative humidity of 50% ± 10%. The mice were provided with ad libitum access to standard laboratory rodent chow and autoclaved drinking water. All animal experiment protocols using mice were approved by the Animal Ethics Committee of Nanjing First Hospital (Nanjing, China, DWSY-24136592) and in accordance with the guidelines for the Care and Use of Laboratory Animals published by the United States National Institutes of Health. All animals were uniformly anesthetized via inhalation of isoflurane (5% for induction, 2% for maintenance) prior to any surgical procedures or euthanasia. The absence of a pedal reflex was confirmed as an indicator of achieving a surgical plane of anesthesia. At the experimental endpoint, animals under deep anesthesia were euthanized by cervical dislocation. Death was confirmed by the permanent cessation of heartbeat and respiration. Every effort was made throughout the study to minimize animal suffering.Orthotopic 4T1 breast cancer models were established in female BALB/c mice. Mice were randomized into four groups (n = 6): 1) PBS, 2) paclitaxel monotherapy, 3) MEVs@CuET monotherapy, and 4) combination therapy. Treatments were administered via tail vein injection for 7 days. Tumor volume and body weight were monitored every other day. On day 28, mice were euthanized, and tumors were excised for H&E, IHC, TUNEL, and immunofluorescence staining.

Blood samples from treated mice were analyzed for routine blood parameters, AST, ALT, urea, creatinine, and CK-MB levels. Major organs were collected for histological examination (H&E staining).

Statistical Analysis

Sample sizes were determined based on established standards and previous studies in the field, and were consistent with or exceeded those reported in comparable preclinical studies to ensure robust detection of treatment effects. Data were analyzed using GraphPad Prism 9. Results are expressed as mean ± SD. One-way ANOVA with Tukey's post hoc test was used for multiple comparisons. Unpaired two-tailed t-tests were used for comparisons between two groups. Significance levels: *P < 0.05, **P < 0.01, ***P < 0.001, ****P < 0.0001, NS: not significant.

Results and Discussion

Preparation and Physicochemical Characterization of MEVs for Efficient Targeting of TNBC Cells

Macrophages possess a natural tropism toward inflammatory and tumor sites, exhibiting high affinity for TNBC tumor cells,[35,40] offering a compelling therapeutic platform for cancer treatment given their superior biocompatibility, immune evasion properties, targeted delivery efficiency, drug protection capacity, multifunctional adaptability, controlled release kinetics, and facile preparation.[41,42] Therefore, this study propose the concept of utilizing macrophage membranes to prepare vesicles. This study treated macrophage cells in the logarithmic growth phase using a rapid freeze-thaw method, followed by ultrasonic treatment to lyse the cell membranes, yielding a large quantity of MEVs. To validate the preservation of native proteins in the extracted membranes, initially conducted Coomassie Brilliant Blue staining on the prepared vesicles. The results confirmed that the membrane-derived extracellular vesicles (MEVs) maintained structural integrity of membrane proteins, as demonstrated in Figure 1a. Subsequently, employed Western blot analysis using CD14, a macrophage-specific surface marker protein, to verify protein enrichment on the vesicular membranes.

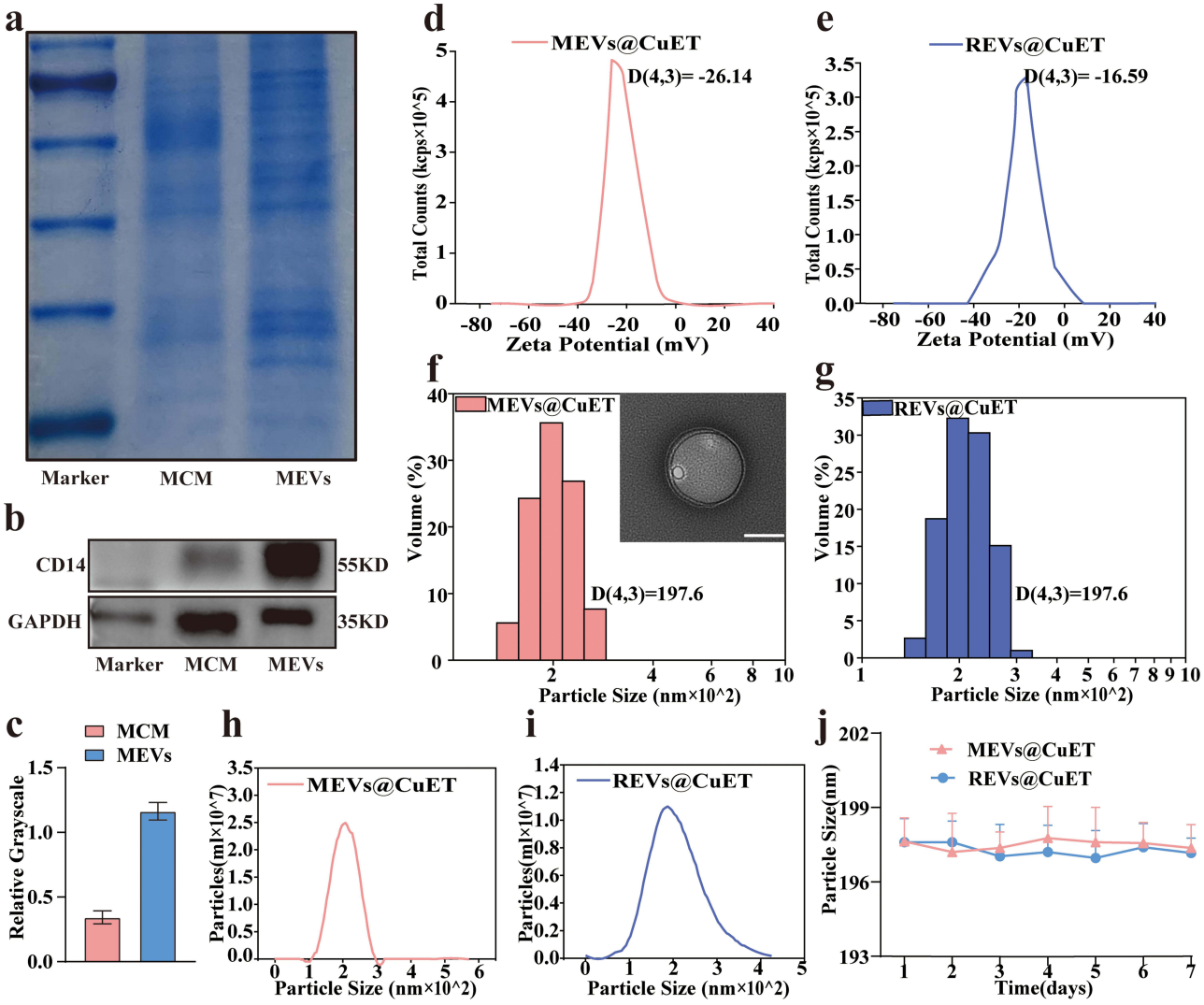

Figure 1 Construction and Characterization of MEVs@CuET. (**a**) Coomassie staining of total proteins from RAW264.7 cell membranes and extracellular vesicles. (**b** and **c**) Electrophoresis and quantification of membrane proteins from RAW264.7 cell membranes and extracellular vesicles. Data are presented as mean ± SD (n = 3). (**d** and **e**) Zeta potential measurements of MEVs@CuET and REVs@CuET. (**f**) TEM and Particle size distribution of MEVs@CuET. Scale bar: 100 nm. (**g**) Particle size distribution of REVs@CuET. (**h** and **i**) Nanoparticle tracking analysis (NTA) characterization of MEVs@CuET and REVs@CuET. (**j**) Changes in particle size of MEVs@CuET and REVs@CuET in culture medium over 7 days. Data are presented as mean ± SD (n = 3).

https://doi.org/10.2147/IJN.S570540

Quantitative analysis of the immunoreactive bands was performed using ImageJ software, as demonstrated in Figure 1b and c. In summary, the extracted MEVs maintained the integrity of membrane proteins and exhibited enrichment of membrane proteins.

The MEVs@CuET with uniform size distribution were successfully fabricated through a combined approach of ultrasonication-assisted incubation and membrane extrusion of CuET-loaded MEVs. Erythrocyte membrane vesicles were used as the control group. As illustrated in Figure 1d and e, the zeta potentials of MEVs@CuET and REVs@CuET were measured to be −26.14 ± 0.60 mV and −16.59 ± 0.95 mV, respectively. Meanwhile, the median diameter of MEVs@CuET was determined to be 197.60 ± 1.11 nm (presented in Figure 1f). The diameter of REVs@CuET was also relatively uniform, with a median diameter of 197.60 ± 1.87 nm (presented in Figure 1g). Transmission electron microscopy (TEM) confirmed that MEVs@CuET exhibited typical vesicular structures with distinct lipid bilayers. Based on the nanoparticle tracking analysis (NTA) results in Figure 1h and i, both MEVs@CuET and REVs@CuET displayed monodisperse size distributions within the nanoscale range, with MEVs@CuET showing a higher particle concentration than REVs@CuET. The MEVs@CuET formulation demonstrated an encapsulation efficiency of 78.2 ± 4.1% and a drug loading capacity of 6.8 ± 0.3%. To further validate the stability, researchers conducted a 7-day in vitro co-culture experiment.Both MEVs@CuET and REVs@CuET exhibited excellent stability, with no significant changes in particle aggregation, as demonstrated in Figure 1j. These results indicate that MEVs@CuET demonstrates robust in vitro stability.

Extracellular vesicles function as natural messengers within cells, facilitating the transport of RNA and proteins between cells.[43,44] Additionally, EVs exhibit remarkable stability in the bloodstream, enabling them to traverse long distances within the body under both physiological and pathological conditions.[45] Their membrane affinity, coupled with the expression of various adhesion proteins such as tetraspanins and integrins on their surface, enhances their ability to fuse with cancer cell membranes and deliver cytotoxic payloads.[46]

To evaluate the efficient uptake of MEVs by 4T1 cells, researchers utilized the cell membrane probe DiI as an indicator to construct MEVs@DiI and REVs@DiI for cell uptake assays and fluorescence co-localization analysis. As displayed in Figure 2a and b, a significant increase in red fluorescence signal was observed in the cytoplasmic region of cells treated with MEVs@DiI after 2, 4, and 6 hours of incubation, demonstrating time-dependent cellular uptake. Furthermore, compared to the control group treated with REVs@DiI, stronger red fluorescence signals were observed in the MEVs@DiI group at all corresponding time points. Subsequent calculation of the co-localization coefficient using ImageJ software revealed a high degree of correlation for MEVs@DiI, reached 25.59 ± 0.15 at 6 hours. Researchers further validated the efficient uptake of MEVs by 4T1 cells using flow cytometry (as illustrated in Figure 2c and d), which was consistent with results by confocal images. In summary, MEVs might potentially serve as effective carriers for CuET delivery and achieving high drug concentrations within tumor cells.

Synergistic Enhancement of Paclitaxel Chemotherapy by MEVs Loaded with CuET in TNBC

Paclitaxel is one of the cornerstone drugs in breast cancer chemotherapy and serves as a first-line treatment option for all molecular subtypes and stages of breast cancer, particularly demonstrating significant efficacy against TNBC. By stabilizing microtubules, paclitaxel inhibits tumor cell division and exhibits notable effects across multiple stages of cancer treatment.[4,5] However, its clinical benefits are substantially limited due to drug resistance and severe adverse reactions.[6,7,47] Cuproptosis, a recently identified form of programmed cell death, is characterized by dysregulated intracellular copper homeostasis.[13] The cytotoxic effects arise from excessive copper ions binding to lipid-acylated components of the tricarboxylic acid (TCA) cycle, ultimately triggering cell death.[14] Beyond its direct cytotoxicity, copper modulates immune cell activity and potentiates antitumor immunity by inducing immunogenic cell death (ICD).[48–52] Given their mitochondrial abundance, breast cancer cells exhibit heightened susceptibility to copper-based agents.[15,17] Building on the demonstrated high affinity of MEVs for breast cancer cells, this study further investigates whether engineered MEVs@CuET can synergistically enhance the therapeutic efficacy of first-line paclitaxel-based chemotherapy.

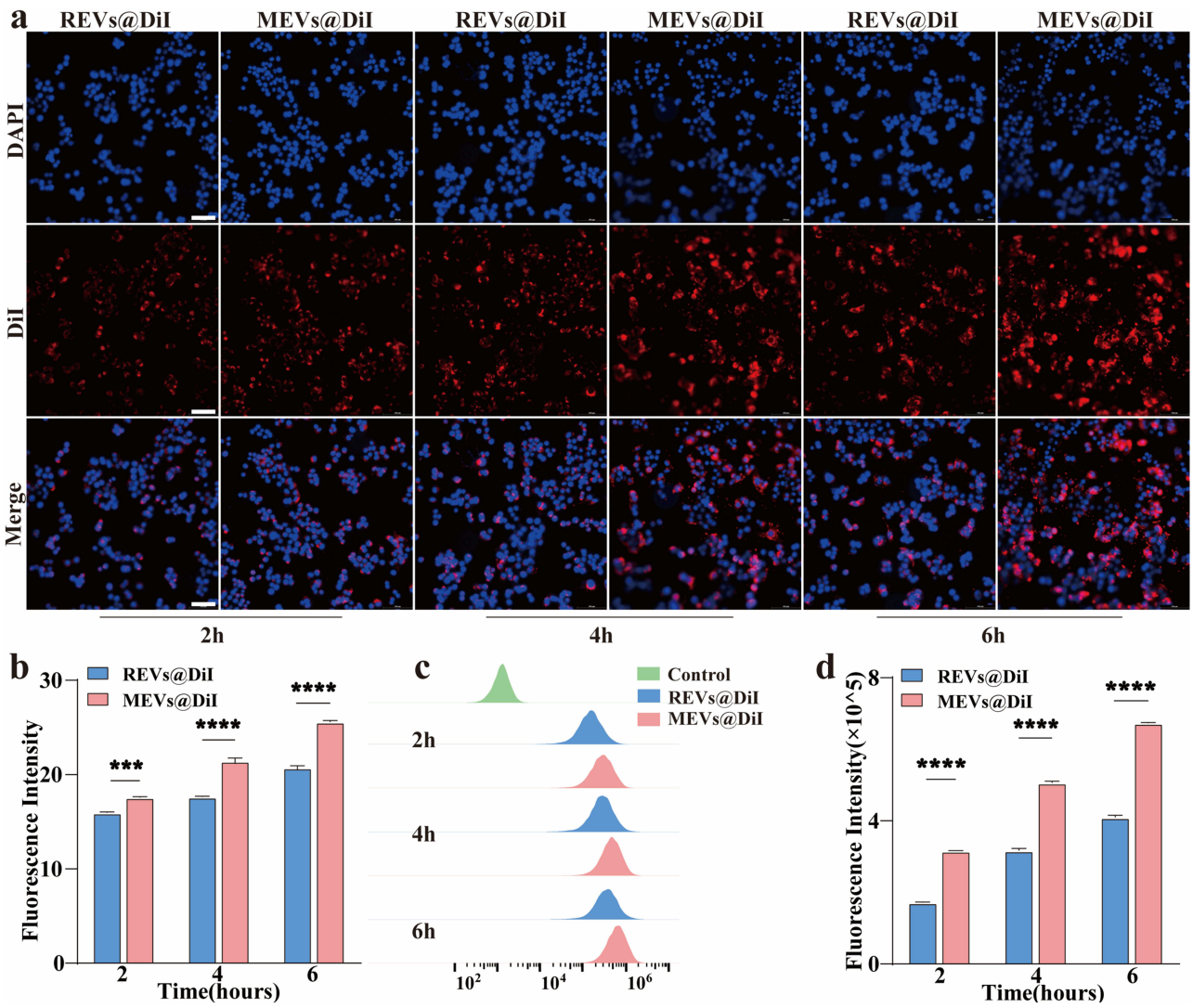

Figure 2 Targeting Effects of MEVs@CuET on Breast Cancer Cells in vitro. (**a** and **b**) Fluorescence microscopy images and semi-quantitative analysis using ImageJ of 4T1 cells co-incubated with MEVs@DiI and REVs@DiI for 2, 4, and 6 hours. Scale bar: 100 μm. (**c** and **d**) Flow cytometry analysis of cellular uptake and semi-quantitative analysis. Data are presented as mean ± SD (n = 3). ***P < 0.001, ****P < 0.0001.

Firstly, the CCK-8 assay was sued to evaluate the cytotoxic effects of paclitaxel, CuET, MEVs@CuET, and REVs@CuET on the 4T1 breast cancer cell line and calculated their half-maximal inhibitory concentrations (IC_{50}). Compared to CuET alone, the MEVs-based delivery system exhibited stronger tumor-killing efficacy, whereas the red blood cell membrane (REVs)-delivered system showed an IC_{50} similar to that of free CuET. Moreover, as the drug concentration increased, the cell viability in the MEVs@CuET-treated group declined more rapidly than in the CuET and REVs@CuET groups. As shown in Figure 3a–d, the IC_{50} values were determined to be 0.39 μg/mL for paclitaxel, and 0.76 μg/mL, 0.37 μg/mL, and 0.69 μg/mL for CuET, MEVs@CuET, and REVs@CuET, respectively. Additionally, we assessed the biosafety of MEVs@CuET on mouse embryonic fibroblast cells (NIH/3T3). The results revealed that even at a high dose of 32.0 μg/mL MEVs@CuET, >97% of NIH/3T3 cells remained viable (Figure S1a).

The above results confirmed the superiority of the MEVs formulation platform in drug delivery. Furthermore, control experiments with empty MEVs (Figure S1b) confirmed the absence of carrier-induced cytotoxicity, providing essential evidence that the observed bioactivity originates specifically from the CuET component. Subsequently, we further evaluated whether this formulation could synergistically enhance the anti-tumor efficacy of paclitaxel. Based on the IC_{50} values of paclitaxel and MEVs@CuET, researchers established a series of drug concentrations and combination

https://doi.org/10.2147/IJN.S570540

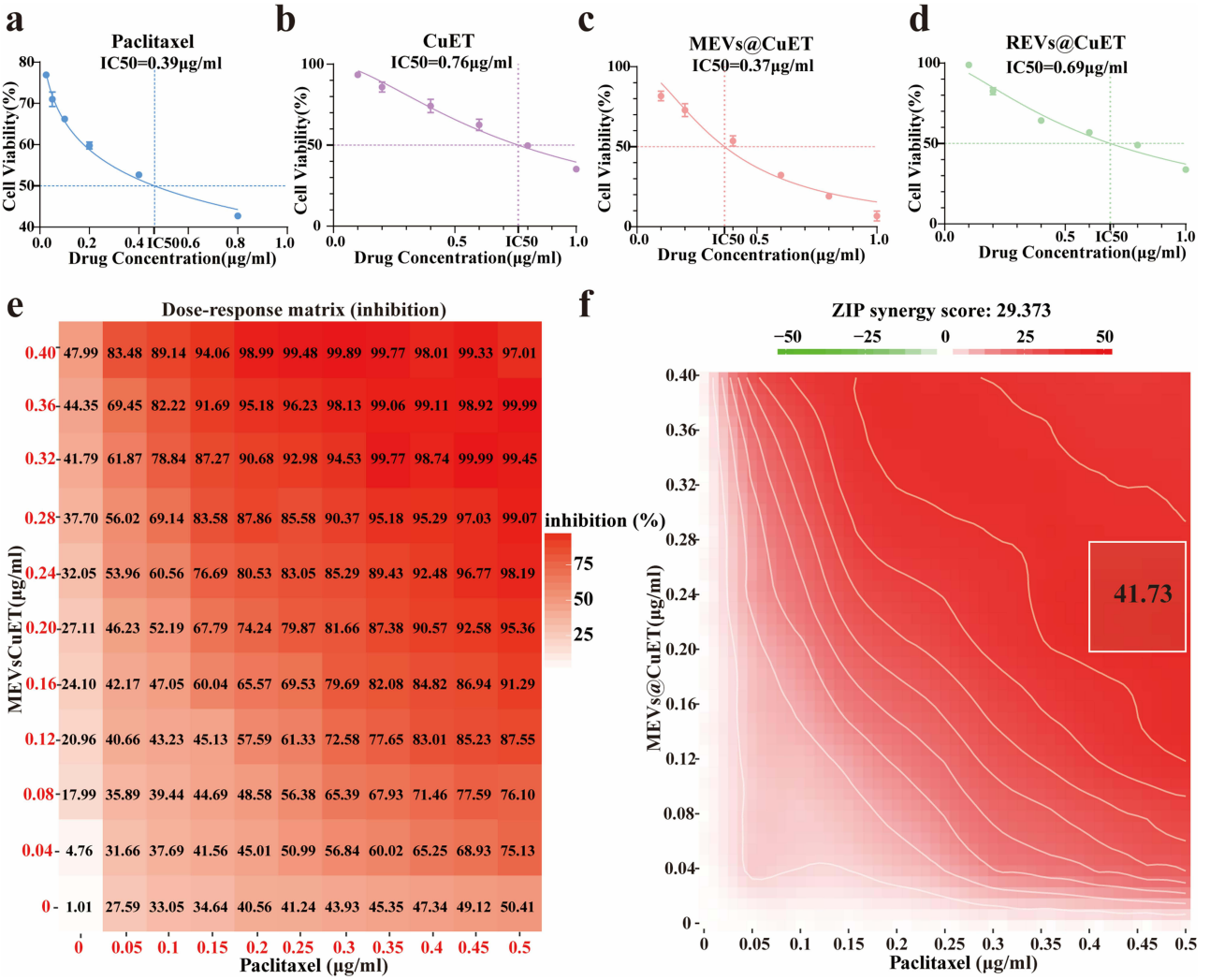

Figure 3 Anti-Tumor Effects of MEVs@CuET and their Synergistic Interaction with Paclitaxel. (**a–d**) Cell viability was measured using the CCK-8 assay to calculate the half-maximal inhibitory concentration (IC_{50}) of paclitaxel, CuET, MEVs@CuET, and REVs@CuET on the breast cancer 4T1 cell line. Data are presented as mean ± SD (n = 6). (**e**) Heatmap of the cell inhibition rates of 4T1 cells treated with varying concentrations and ratios of paclitaxel and MEVs@CuET, as measured by the CCK-8 assay. (**f**) Synergy heatmap of the combined effects of paclitaxel and MEVs@CuET, calculated using SynergyFinder 3.0. Data are presented as mean ± SD (n = 3).

ratios with 10% intervals. The cell inhibition rates were then quantitatively evaluated using the CCK-8 assay, and the corresponding data (including inhibition rates and drug concentrations) were formatted and imported into SynergyFinder 3.0 (https://synergyfinder.fimm.fi) for analysis.SynergyFinder is a freely available web tool for interactive analysis and visualization of multi-drug combination response data.[53–55] In this study, researchers employed the ZIP model for analysis, where higher synergy scores indicate stronger synergistic effects. Scores greater than 10 represent significant synergy, scores between −10 and 10 indicate no significant interaction, and scores below −10 denote significant antagonism.

Based on the results from SynergyFinder, the dose-response curves for paclitaxel and MEVs@CuET are represented in Figure S2a and S2b, consistent with the IC_{50} values calculated in previous experiments. The tumor-killing efficacy of the combination therapy was significantly stronger than that of either drug alone, with the effect increasing at higher drug concentrations, as shown in Figure 3e, where deeper red indicates stronger cell inhibition. The ZIP model calculated a synergy score of 29.37 ($p < 0.05$), with the highest regional synergy score reaching 41.73, as presented in Figure 3f and Figure S3, provide a more intuitive visualization of the synergistic effects at different doses and ratios. The heatmap shows predominantly red regions, with deeper red at higher concentrations, indicating stronger synergy. The 3D plot also

demonstrates that the synergistic effect increases with concentration. These findings suggest that MEVs@CuET and paclitaxel exhibit synergistic effects, with the synergy becoming more pronounced at higher concentrations, likely through complementary mechanisms that enhance therapeutic efficacy.

The results of preliminary experiments confirmed the synergistic effects of combining MEVs@CuET with paclitaxel. Therefore, researchers selected a dose with a high synergy index and appropriate drug concentrations for investigating antitumor drug efficacy in vitro, with paclitaxel and MEVs@CuET concentrations set at 0.13 μg/mL and 0.25 μg/mL, respectively. After treating 4T1 cells with the selected combination dose, researchers performed live/dead cell staining using calcein-AM/PI and observed the cells under a fluorescence microscope, as evidenced by Figure 4a and b. In the control group, tumor cells exhibited strong viability, with almost all cells displaying green fluorescence and minimal dead cells. Compared to the paclitaxel and MEVs@CuET monotherapy groups, the combination therapy group showed significantly more dead cells. Semi-quantitative analysis using ImageJ software revealed that the average optical density of viable 4T1 cells in the MEVs@CuET, paclitaxel monotherapy, and combination therapy groups was 68.00 ± 2.00%, 75.30 ± 1.53%, and 51.67 ± 2.08%, respectively.

Subsequently, researchers evaluated the apoptotic effects of paclitaxel, MEVs@CuET monotherapy, and their combination by FACS at 24 hours-post administration. Flow cytometry analysis showed that the control group had an average apoptosis rate of 6.17 ± 0.37%, while the MEVs@CuET and paclitaxel monotherapy groups exhibited average apoptosis rates of 32.20 ± 1.41% and 32.17 ± 0.25%, respectively. In contrast, the combination therapy group demonstrated a significantly higher average apoptosis rate of 54.33 ± 0.87% ($p < 0.0001$), as shown in Figure 4c and d. In summary, the combination of MEVs@CuET with paclitaxel exhibited significantly stronger anti-tumor effects compared to monotherapy and effectively promoted tumor cell apoptosis.

Integrated Transcriptomic and Functional Analysis Unveils Immune-Related Mechanisms of Synergistic Therapy with MEVs@CuET and Paclitaxel

To further explore the potential mechanisms by which the combination of MEVs@CuET and paclitaxel enhances anti-tumor efficacy, researchers performed transcriptome sequencing and bioinformatics analysis. In brief, 4T1 breast cancer cells were treated with paclitaxel, MEVs@CuET, or their combination and the total RNA was extracted after 24 hours. Library construction was performed using the Illumina® Stranded mRNA Prep, Ligation method, followed by sequencing on the NovaSeq X Plus platform. High-quality sequencing data (clean data) were obtained after filtering the second-generation high-throughput sequencing data for subsequent analysis. The paclitaxel monotherapy group was set as the control.

Volcano plot analysis revealed a total of 1,003 differentially expressed genes (DEGs) between the PTX and combination therapy groups, including 196 upregulated and 807 downregulated genes (Figure 5a). The heatmap further confirmed significant genetic differences between the two groups (Figure S4). Subsequently, Gene Ontology (GO), Kyoto Encyclopedia of Genes and Genomes (KEGG), and Reactome Pathway Browser databases were used to analyze the biological processes, metabolic pathways, and pathways enriched by the DEGs. GO analysis indicated that the DEGs were primarily enriched in molecular functions and biological processes such as nucleosome assembly, nuclease activity, and viral entry into host cells (Figure 5b). Reactome analysis revealed significant enrichment of DEGs in pathways related to chromatin modification, DNA repair, and epigenetic regulation (Figure 5c), suggesting that these genes may be involved in regulating chromatin structure, DNA repair, and epigenetic processes. KEGG analysis, represented by a bubble plot, showed that the DEGs were mainly enriched in pathways related to immune regulation, inflammatory responses, and autoimmune diseases. Notably, the cytokine-cytokine receptor interaction pathway and the IL-17 signaling pathway were prominently enriched (Figure 5d), indicating that the DEGs may play a role in immune regulation, inflammatory responses, and the pathogenesis of autoimmune diseases.

Based on these findings, in vitro investigations were conducted to examine the IL-17 cytokine signaling pathway under different drug treatments. Specifically, IL-17 levels and Th17 cell populations were measured, with the detailed experimental protocol illustrated in Figure 5e. Initially, lymphocytes were isolated from the spleens of healthy mice and subsequently cultured in conditioned medium from drug-treated 4T1 cells. After 48 hours, the supernatant was collected,

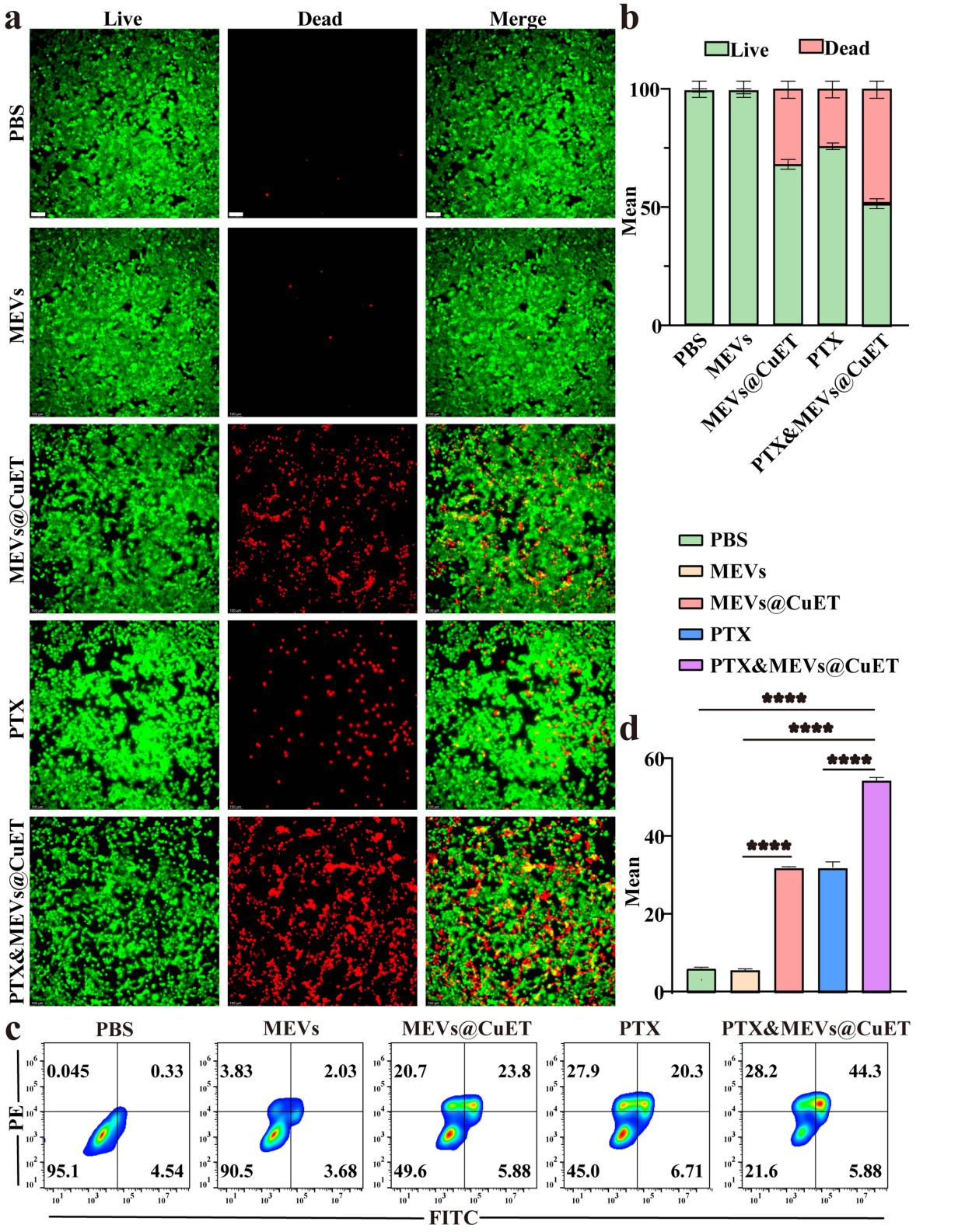

Figure 4 Anti-Tumor Effects of MEVs@CuET in Combination with Paclitaxel in vitro. (**a**) 4T1 cells were treated with 0.13 μg/mL paclitaxel and 0.25 μg/mL MEVs@CuET individually or in combination for 24 hours, followed by live/dead cell staining. Fluorescence microscopy images were captured. Scale bar of 100 μm. (**b**) Semi-quantitative analysis of live/dead staining in 4T1 cells using ImageJ. (**c** and **d**) Apoptosis detection and semi-quantitative analysis of 4T1 cells treated with monotherapy or combination therapy for 24 hours, as assessed by flow cytometry. Data are presented as mean ± SD (n = 3). ****P < 0.0001.

https://doi.org/10.2147/IJN.S570540

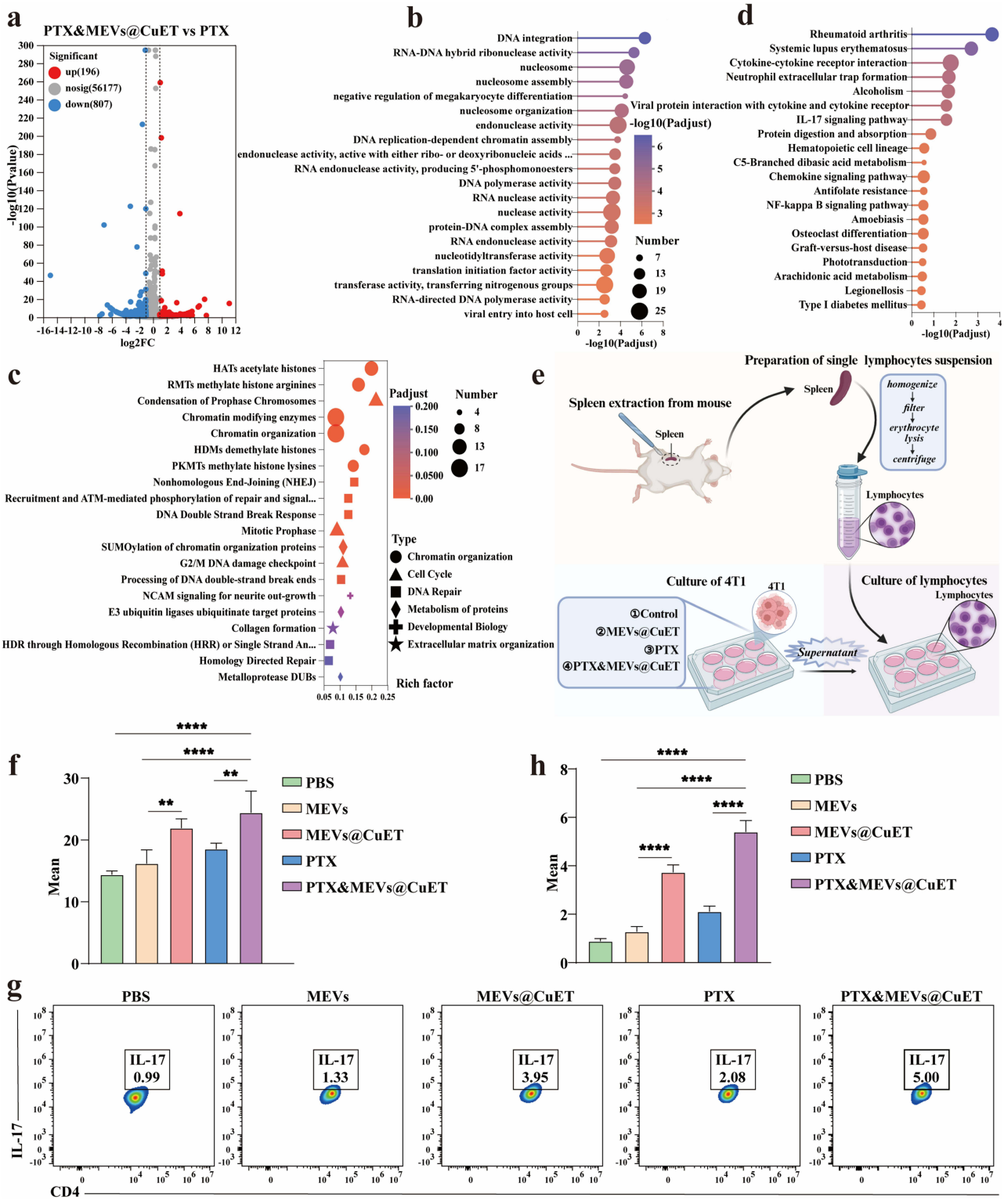

Figure 5 MEVs@CuET Enhances the Anti-Tumor Efficacy of Paclitaxel Through Immunomodulation. (**a**) Volcano plot of differentially expressed genes (DEGs) in 4T1 cells treated with paclitaxel (PTX) monotherapy versus combination therapy. (**b**) GO enrichment analysis of DEGs in 4T1 cells treated with PTX monotherapy versus combination therapy. (**c**) Reactome enrichment analysis of DEGs in 4T1 cells treated with PTX monotherapy versus combination therapy. (**d**) KEGG enrichment analysis of DEGs in 4T1 cells treated with PTX monotherapy versus combination therapy. (**e**) Schematic diagram of the in vitro experimental design for investigating IL-17 cytokine signaling pathway regulation under different drug treatments. (**f**) ELISA measurement of IL-17 levels in the supernatant of cultured splenic lymphocytes from healthy mice. (**g** and **h**) Flow cytometry detection and quantification of Th17 cell levels in splenic lymphocytes from healthy mice after incubation with conditioned media from drug-treated 4T1 cells. Data are presented as mean ± SD (n = 6). **P < 0.01, ****P < 0.0001.

https://doi.org/10.2147/IJN.S570540

and IL-17 levels were measured using enzyme-linked immunosorbent assay (ELISA). As represented in Figure 5f, the combination therapy group exhibited significantly higher IL-17 levels compared to the paclitaxel monotherapy group ($p < 0.01$). The average IL-17 concentrations in the control, MEVs, MEVs@CuET, paclitaxel, and combination therapy groups were 14.39 ± 0.61 pg/mL, 16.18 ± 2.22 pg/mL, 21.90 ± 1.50 pg/mL, 18.54 ± 0.94 pg/mL, and 24.42 ± 3.49 pg/mL, respectively. Additionally, researchers performed flow cytometry on the cultured mouse splenic lymphocytes after 48 hours. Lymphocytes were labeled with surface antibodies against CD3, CD4, and CD45, followed by permeabilization and staining with an IL-17 antibody to detect Th17 lymphocytes. As shown in Figure 5g and h, the combination therapy group showed a significant increase in Th17 lymphocyte levels compared to the paclitaxel monotherapy group ($p < 0.0001$). The average Th17 lymphocyte percentages in the control, MEVs, MEVs@CuET, paclitaxel, and combination therapy groups were 0.88 ± 0.11%, 1.28 ± 0.21%, 3.73 ± 0.31%, 2.11 ± 0.23%, and 5.40 ± 0.48%, respectively, consistent with the observed IL-17 concentration trends. IL-17, a pivotal pro-inflammatory cytokine predominantly secreted by Th17 cells, plays crucial roles in diverse pathological conditions including autoimmune diseases, infectious diseases, malignancies, cardiovascular disorders, and respiratory ailments.[56–59] Emerging evidence indicates that IL-17 potentiates anti-tumor immune responses through recruitment and activation of immune cells (eg, neutrophils and T lymphocytes). Furthermore, it may suppress regulatory T cell (Treg) function, thereby relieving their inhibitory effects on effector T cells.[60] Collectively, these results suggest that MEVs@CuET enhances the anti-tumor effects of paclitaxel by modulating the IL-17 signaling pathway.

Spatial Distribution Patterns of MEVs@CuET in vivo

Regarding the affinity of MEVs to TNBC and their synergistic anti-tumor effect with paclitaxel, the above experiments have been verified in vitro. In order to further evaluate whether MEVs@CuET can exhibit better therapeutic effects in vivo, the characteristics of the in vivo distribution of MEVs were first studied. The near-infrared probe IR-780 was used to label MEVs@CuET and REVs@CuET, with unbound IR-780 as control. Biodistribution was tracked at 2–-24 h after tail vein injection.

As shown in Figure 6a and b, MEVs@CuET/IR 780 exhibited significant accumulation at the tumor site within 2 hours, with fluorescence intensity increasing over time. The highest fluorescence intensity at the tumor site was observed at 24 hours. In contrast, REVs@CuET/IR 780 showed delayed and weaker fluorescence, with minimal accumulation at the tumor site only after 12 hours. Subsequently, tumor tissues and organs were excised to examine the distribution patterns of MEVs@CuET. As shown in Figure 6a and c, the isolated tumor tissues displayed the highest fluorescence intensity for MEVs@CuET, with concentrations 2.16-fold higher than the REVs@CuET/IR 780 group and 4.38-fold higher than the IR 780 group. Furthermore, fluorescence signals were predominantly localized in tumor tissues with minimal distribution in major organs.These results demonstrate the ability of MEVs@CuET to accumulate at tumor sites, thereby avoiding off-target effects and reducing systemic adverse reactions.

In vivo Antitumor Efficacy and Immune Modulation by MEVs@CuET Combined with Paclitaxel in an Orthotopic TNBC Mouse Model

An orthotopic 4T1 breast cancer model was established in BALB/c mice by injecting 4T1 cells into the mammary fat pads. Seven days later, the mice were divided into four treatment groups and administered treatments for seven consecutive days, followed by a 15-day observation period (Figure 7a). The four treatment groups included: PBS, paclitaxel monotherapy, MEVs@CuET monotherapy, and a combination of paclitaxel and MEVs@CuET. Tumor growth curves are presented in Figure 7b, and the size of excised tumors is displayed in Figure 7c. Compared to the PBS group, the average tumor inhibition rates on day 28 for the MEVs@CuET monotherapy, paclitaxel monotherapy, and combination therapy groups were 45.74%, 39.79%, and 91.47%, respectively, as shown in Figure 7d.

Subsequently, histological studies were conducted to assess in vivo toxicity and anti-tumor efficacy. Tumor tissues were stained with H&E, anti-Ki67, anti-Bcl2, and TUNEL. As displayed in Figure 7e, H&E staining revealed tightly packed tumor cells with visible mitotic figures in the PBS group, while the combination therapy group exhibited reduced cellularity, tissue fibrosis, nuclear pyknosis, fragmentation, and dissolution, indicating features of apoptosis and necrosis.

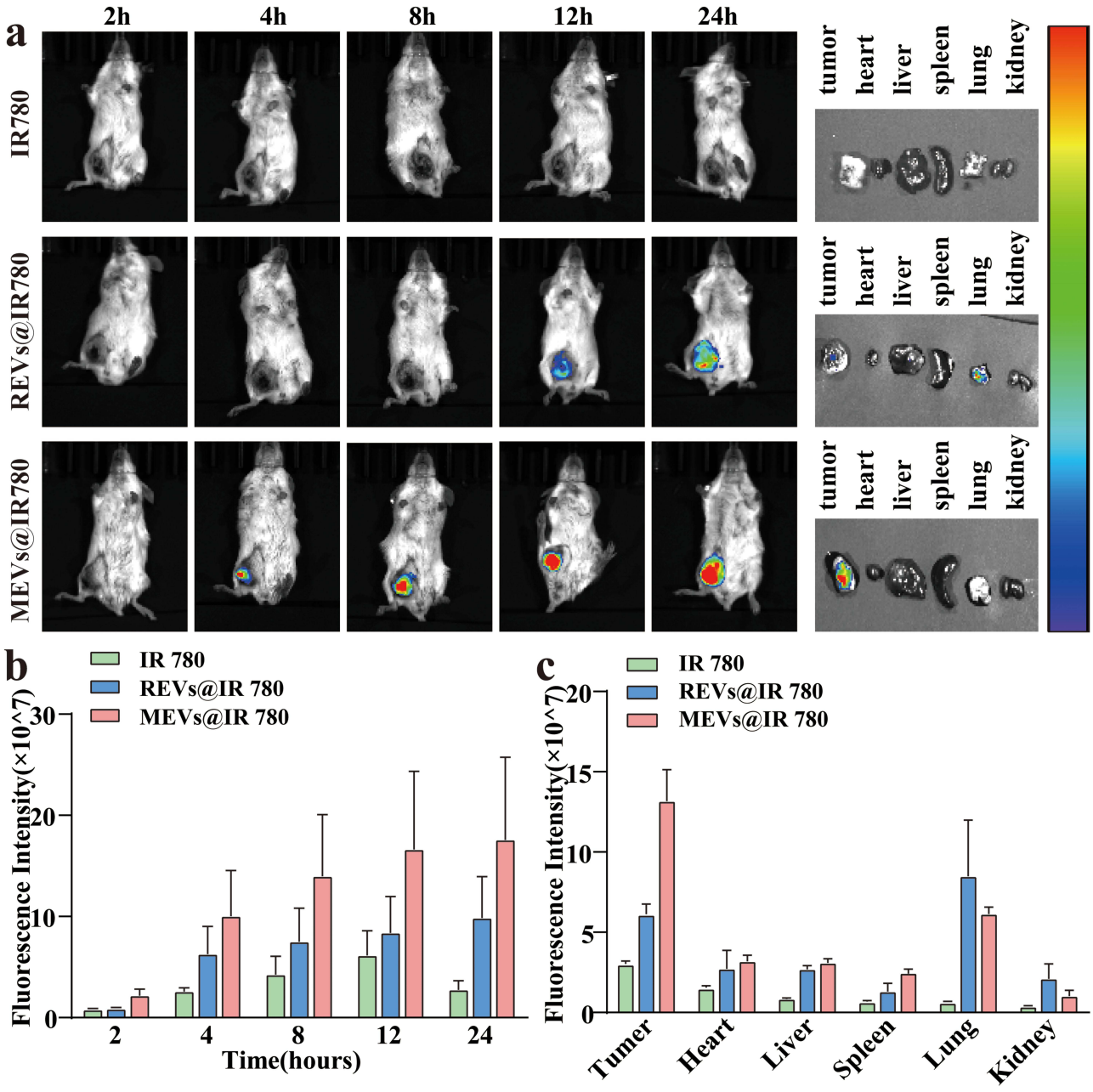

Figure 6 Spatial Distribution Patterns of MEVs@CuET in vivo. (**a**) Fluorescence imaging of mice at 2, 4, 8, 12, and 24 hours post-intravenous injection using an in vivo imaging system. Tumor and major organs were collected for fluorescence imaging at 24 hours post-injection. (**b** and **c**) Semi-quantitative analysis of fluorescence intensity in mouse tumors and organs. Data are presented as mean ± SD (n = 3).

Immunohistochemical analysis of Ki67, a marker of cell proliferation, showed that the percentage of Ki67-positive cells decreased by 30.20% and 24.65% in the MEVs@CuET and paclitaxel monotherapy groups, respectively, compared to the PBS group (Figure 7f and g). In contrast, the combination therapy group demonstrated a significant reduction in Ki67 positivity by approximately 52.10%, representing a 36.43% decrease compared to the paclitaxel monotherapy group. This indicates that the combination of paclitaxel and MEVs@CuET has significantly stronger anti-tumor efficacy than monotherapy.

Additionally, researchers analyzed the anti-apoptotic levels in tumor tissues using immunohistochemistry, as shown in Figure 7h and i. Bcl-2, a key anti-apoptotic protein, plays a critical role in apoptosis, cancer, and other diseases.[61–63] The combination therapy group showed a significant reduction in Bcl-2 expression, decreasing by 69.01% compared to the

https://doi.org/10.2147/IJN.S570540

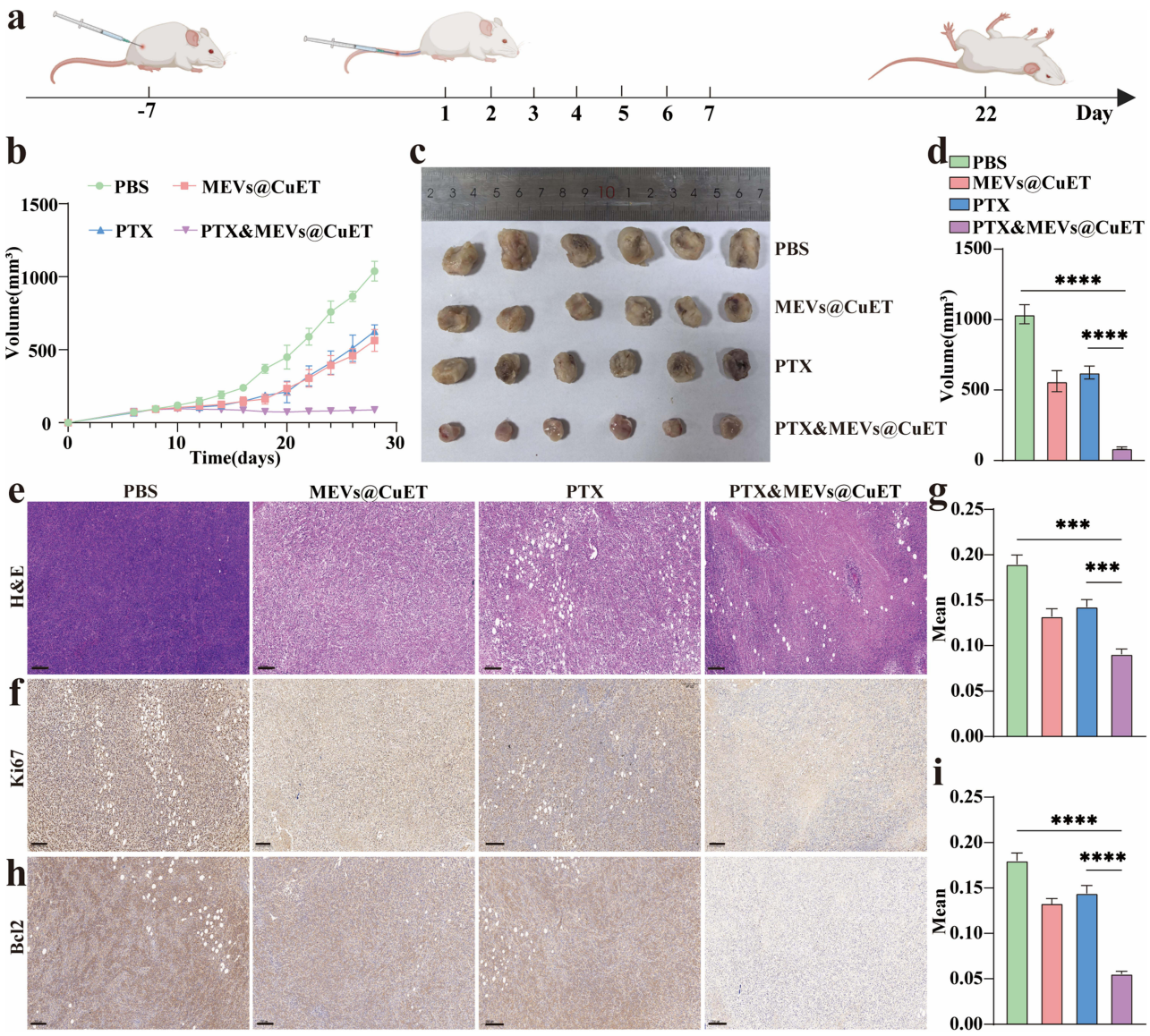

Figure 7 Anti-Tumor Effects and Mechanisms of MEVs@CuET in Combination with Paclitaxel in vivo. (**a**) Schematic illustration of in vivo therapeutic treatment in orthotopic 4T1 breast cancer mouse model. (**b**) The tumor size changes in mice from the PBS group, MEVs@CuET monotherapy group, paclitaxel monotherapy group and the combination therapy group of paclitaxel and MEVs@CuET. The tumors were observed over 28 days, with recordings taken every 2 days. (**c** and **d**) Images and statistical analysis of tumor size from the excised tumors of mice in the four treatment groups after euthanasia. (**e**) H&E staining of excised tumors from mice in the four treatment groups. (**f** and **g**) Ki-67 staining and expression level semi-quantitative analysis using ImageJ for excised tumors from mice in the four treatment groups. (**h** and **i**) Bcl2 staining and expression level semi-quantitative analysis using ImageJ for excised tumors from mice in the four treatment groups. Scale bar: 200 μm. Data are presented as mean ± SD (n = 6). ***P < 0.001, ****P < 0.0001.

PBS group and by 61.30% compared to the paclitaxel monotherapy group. TUNEL staining revealed a significant increase in apoptotic cells in the combination therapy group, approximately 197.52-fold higher than the PBS group and 1.80-fold higher than the paclitaxel monotherapy group (Figure S5). These results are consistent with the in vitro anti-tumor efficacy experiments.

T cell subsets play pivotal roles in the tumor immune microenvironment, with Th17 cells and their signature cytokine IL-17 demonstrating the capacity to promote anti-tumor immunity. Th17 cells facilitate T cell infiltration and dendritic cell (DC) maturation through IL-17 secretion, while simultaneously activating stromal cells and myeloid cells. Furthermore, IL-17 can regulate the differentiation, functionality, and stability of Th17 cells via positive feedback loops or paracrine mechanisms. Building upon prior transcriptomic and in vitro evidence that MEVs@CuET potentiates paclitaxel's antitumor effects via IL-17 pathway modulation, the in vivo immune landscape was characterized. Th17 cells, a subset of $CD4^+$

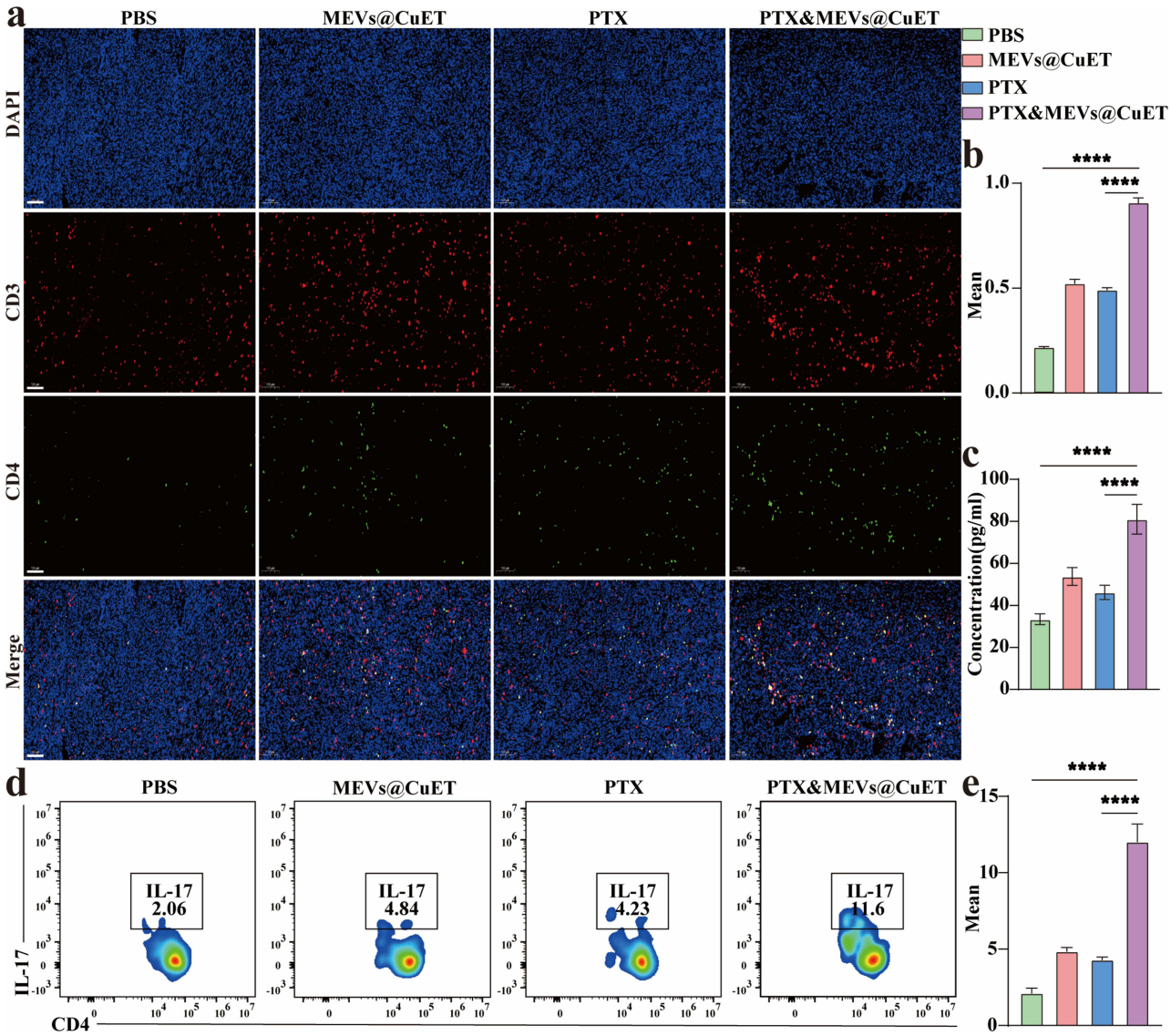

Figure 8 Anti-Tumor Effects and Mechanisms of MEVs@CuET in Combination with Paclitaxel in vivo. To evaluate immune indicators in mice, immunofluorescence double staining for CD3 and CD4 was performed on excised tumor tissues from mice in the PBS group, MEVs@CuET monotherapy group, paclitaxel monotherapy group, and the combination therapy group of paclitaxel and MEVs@CuET. Additionally, the concentration of IL-17 in the peripheral blood serum of mice from the four treatment groups was measured using ELISA, and the Th17 cell content in the spleen was analyzed using flow cytometry. (**a** and **b**) CD3 and CD4 immunofluorescence double staining and fluorescence intensity semi-quantitative analysis using ImageJ for excised tumors from mice in the four treatment groups. Scale bar: 100 μm. (**c**) IL-17 concentration in the peripheral blood serum of mice from the four treatment groups. (**d** and **e**) Th17 cell content in splenic lymphocytes of mice from the four treatment groups, detected by flow cytometry and quantified. Data are presented as mean ± SD (n = 6). ****P < 0.0001.

T cells, were evaluated in tumor tissues using immunofluorescence. As displayed in Figure 8a and b, the combination therapy group exhibited a significant increase in $CD4^+$ T cells, approximately 4.21-fold higher than the PBS group and 1.84-fold higher than the paclitaxel monotherapy group. Furthermore,IL-17 levels in the peripheral blood serum of mice were measured using ELISA. As shown in Figure 8c, the combination therapy group showed a significant increase in IL-17 concentration, approximately 2.42-fold higher than the PBS group and 1.75-fold higher than the paclitaxel monotherapy group. Additionally, splenic lymphocytes were isolated from the mice and analyzed by flow cytometry to quantify Th17 cell populations, enabling further investigation of systemic immune modulation in vivo. As illustrated in Figure 8d and e, the combination therapy group exhibited elevated Th17 cell levels. These findings align with the in vitro results, suggesting that MEVs@CuET enhances the anti-tumor effects of paclitaxel by modulating the immune response, particularly through the IL-17 signaling pathway.

https://doi.org/10.2147/IJN.S570540

In vivo Safety Evaluation of MEVs@CuET Combined with Paclitaxel in Tumor-Bearing Mice

To evaluate the in vivo safety of the treatments, researchers performed routine and biochemical tests on the mice post-treatment. The complete blood count results, as represented in Figure 9a–c and Figure S6, revealed no significant reduction in the three major blood cell lineages (red blood cells, white blood cells, and platelets) in any of the treatment groups, including the combination therapy group, monotherapy groups, and PBS group, with no statistically significant differences between groups ($p > 0.05$). However, an increase in lymphocyte percentage and a decrease in neutrophil percentage were observed in the combination therapy group compared to the PBS group ($p < 0.05$), though no significant difference was noted compared to the paclitaxel monotherapy group ($p > 0.05$). This may be attributed to the potent immunomodulatory effects of the combination therapy. Additionally, no significant abnormalities were observed in liver function (ALT, AST), kidney function (Urea, Crea), or cardiac injury markers (CK-MB), with no statistically significant differences between groups ($p > 0.05$), as represented in Figure S6.

Furthermore, body weight was monitored throughout the study. The weight curves indicated no significant differences between the monotherapy and combination therapy groups, and no notable weight loss was observed during the treatment period, as shown in Figure 9d. Interestingly, a slight increase in body weight was observed in the tumor-bearing mice from the combination therapy group in the later stages, further confirming the high safety profile of the combined treatment in vivo. Finally, the heart, liver, spleen, lungs, and kidneys were collected from euthanized mice for hematoxylin and eosin (H&E) staining. As displayed in Figure 9e, no abnormalities were observed in the tissues from any of the four groups, and no signs of liver or kidney toxicity were detected, reaffirming the high safety of this treatment regimen.

Discussion

Breast cancer remains the most prevalent malignancy among women worldwide, accounting for approximately 25% of all female cancer cases.[64] Despite remarkable advances in targeted therapies and immunotherapies—such as HER2-targeted agents and immune checkpoint inhibitors (eg, PD-1/PD-L1 blockers)—chemotherapy, particularly paclitaxel-based regimens, continues to serve as a first-line treatment for various subtypes of breast cancer. However, its clinical efficacy is often compromised by low response rates, dose-limiting toxicities, and the development of drug resistance. Therefore, identifying strategies that can sensitize tumor cells to chemotherapeutic agents is of critical importance.

Targeted drug delivery represents a key approach to improving the therapeutic index of chemotherapy. In recent years, cell-mimetic nanocarriers have emerged as promising tools due to their excellent biocompatibility, prolonged circulation time, and intrinsic tumor-homing properties. Among these, macrophage-derived extracellular vesicles (MEVs) have attracted increasing attention owing to their natural ability to infiltrate tumor tissues and evade immune clearance. Paclitaxel, while widely used for its microtubule-stabilizing properties, faces limitations in clinical settings, especially in tumors exhibiting intrinsic or acquired resistance. Therefore, exploring molecular mechanisms that can enhance its sensitivity offers significant translational potential. Cuproptosis, through the accumulation of copper ions and subsequent mitochondrial dysfunction, presents a novel avenue for selectively eliminating cancer cells. Building on advantages of MEVs, we developed CuET, a copper(II)-chelating agent capable of inducing cuproptosis, loading platform (MEVs@CuET) for combining CuET-mediated cuproptosis with paclitaxel could generate synergistic antitumor effects.

Our findings demonstrated that MEVs@CuET effectively delivered CuET to tumor cells both in vitro and in vivo, achieving faster and more sustained tumor accumulation compared to red blood cell-derived vesicles (REVs@CuET). Importantly, in vitro cytotoxicity assays using NIH/3T3 fibroblasts showed minimal off-target toxicity, while in vivo safety assessments revealed no significant alterations in hematological or biochemical parameters, indicating the biocompatibility of this formulation. When combined with paclitaxel, MEVs@CuET exhibited strong synergistic antitumor activity, as evidenced by a synergy score of 29.37 (ZIP model), with peak regional scores reaching 41.73. Functional assays confirmed enhanced inhibition of tumor cell proliferation and increased apoptosis. In vivo studies further demonstrated significantly improved tumor growth suppression in the combination group, supported by reduced Ki67 expression and elevated TUNEL staining and Bax/Bcl-2 ratio in treated tumors.

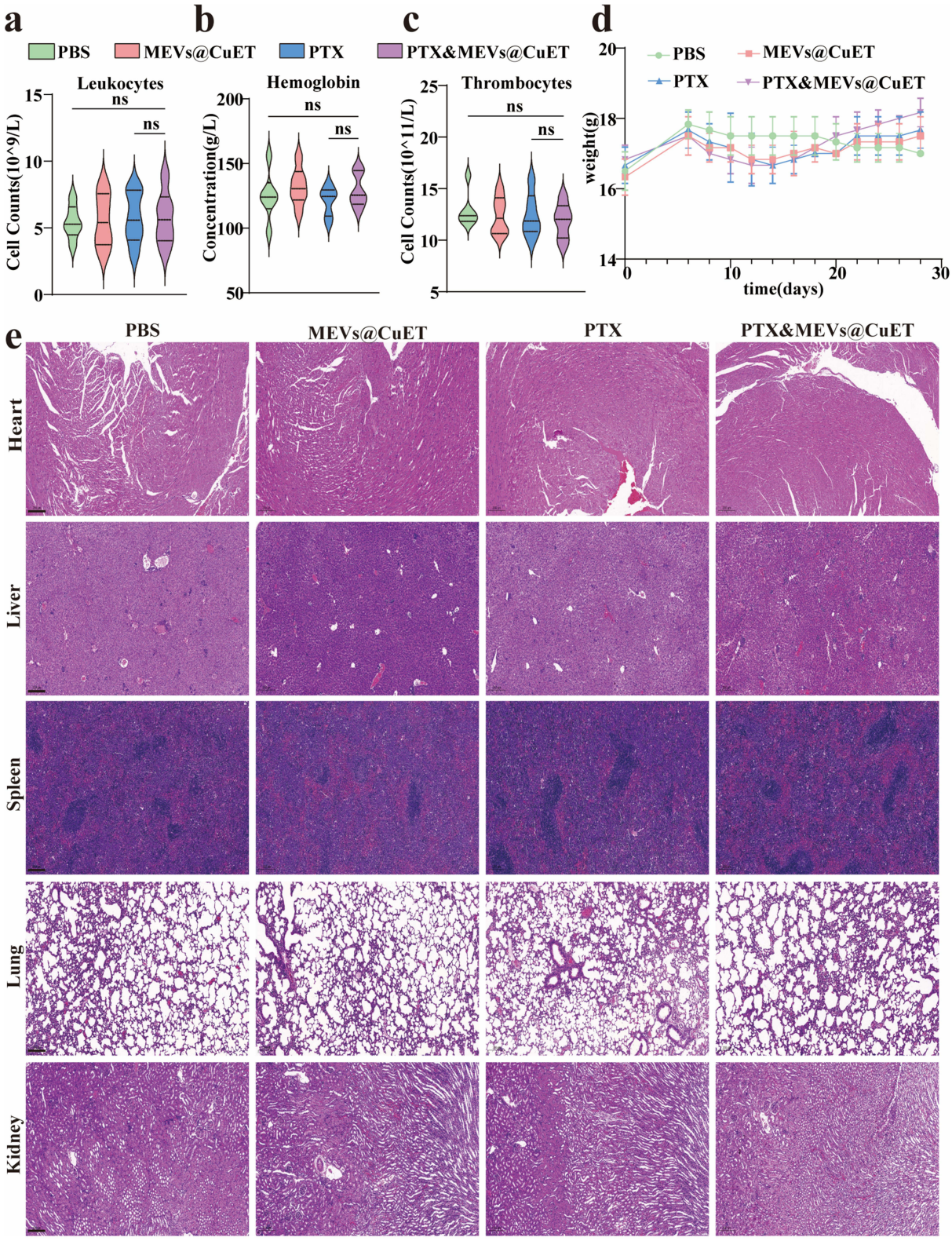

Figure 9 Safety of MEVs@CuET in Combination with Paclitaxel in vivo. (**a–c**) White blood cell count, hemoglobin concentration, and platelet count in the peripheral blood of mice from the PBS group, MEVs@CuET monotherapy group, paclitaxel monotherapy group and the combination therapy group of paclitaxel and MEVs@CuET. (**d**) Body weight change curves of mice in the four groups over 28 days, recorded every 2 days. (**e**) After euthanizing the mice from the four treatment groups, the heart, liver, spleen, lungs, and kidneys were collected and subjected to H&E staining. Scale bar: 200 μm. Data are presented as mean ± SD (n = 6).
Abbreviation: ns, not significant.

https://doi.org/10.2147/IJN.S570540

To explore the underlying mechanisms, we performed transcriptome sequencing of 4T1 cells treated with the respective formulations. Pathway analysis revealed significant enrichment in immune-related pathways, particularly the IL-17 signaling pathway. Flow cytometric analysis of splenic lymphocytes co-cultured with conditioned media from drug-treated tumor cells showed elevated levels of Th17 cells, accompanied by increased IL-17 secretion as measured by ELISA. Consistent results were observed in vivo, where combination therapy led to higher serum IL-17 levels and increased infiltration of $CD4^+$ T cells within the tumor microenvironment (approximately 1.84-fold increase compared to paclitaxel monotherapy). Copper ions are increasingly recognized as important regulators in the tumor microenvironment, capable of modulating immunogenic cell death (ICD) via reactive oxygen species (ROS) generation and damage-associated molecular pattern (DAMP) release.[65] Emerging evidence suggests that copper-induced ICD may potentiate anti-tumor immunity and improve responses to chemo- and immunotherapy.[66] Our findings support the hypothesis that the combination of cuproptosis induction and microtubule stabilization not only enhances direct tumor cell killing but also activates a robust adaptive immune response.

While this study demonstrates the promising therapeutic potential of MEVs@CuET in overcoming paclitaxel resistance, several limitations should be acknowledged. First, although our in vitro experiments with empty MEV controls clearly attribute the observed cytotoxicity and IL-17/Th17 activation to CuET, future studies that include corresponding in vivo empty-vesicle controls would further strengthen this conclusion by accounting for the complexity of the tumor microenvironment. Second, although our findings strongly link cuproptosis induction to IL-17/Th17 axis activation, the exact molecular signaling cascade that connects this cell death process to adaptive immunity remains to be fully elucidated. The observed link suggests a novel immunomodulatory function of copper-induced cell death. We hypothesize that this immune activation may occur through the release of DAMPs such as ATP and HMGB1, which can promote dendritic cell maturation and Th17 polarization.[67–69] Alternatively, copper stress may modulate key inflammatory pathways (eg, NF-κB or MAPK) within the tumor microenvironment to favor an IL-17-prone milieu.[70–72] Unraveling this precise mechanistic link represents an important avenue for future investigation. Finally, the clinical translation of this biomimetic strategy faces practical challenges, including the scalable production and quality control of macrophage-derived vesicles, comprehensive evaluation of long-term biocompatibility and pharmacokinetics, and potential patient stratification based on tumor copper metabolism or immune phenotypes. Addressing these issues will be essential for advancing this therapeutic paradigm toward clinical application.

Conclusions

In conclusion, this study demonstrates that macrophage-derived vesicles can serve as effective nanocarriers for targeted delivery of cuproptosis inducers. The combination of MEVs@CuET with paclitaxel synergistically suppresses tumor growth through dual mechanisms: direct inhibition of cell proliferation and activation of IL-17-mediated anti-tumor immunity. These findings highlight the therapeutic potential of integrating novel cell death modalities with conventional chemotherapy and provide a promising strategy for overcoming drug resistance in breast cancer. Moreover, the observed modulation of the IL-17/Th17 axis suggests potential relevance for cancers associated with autoimmune conditions or for managing immune-related adverse events, where precise regulation of this pathway may offer therapeutic benefits. Future studies should aim to further elucidate the molecular interplay between cuproptosis and immune activation, as well as explore the clinical translation of such combinatory approaches.

Abbreviations

BC, Breast cancer; Bcl2, B-cell lymphoma 2; CAFs, Cancer-associated fibroblasts; CAR-T, Chimeric Antigen Receptor T-Cell; CTLA-4, Cytotoxic T-Lymphocyte-Associated Protein 4; CuET, Copper(II) bis(diethyldithiocarbamate); CCK-8, Cell Counting Kit-8; DAMPs, Damage-Associated Molecular Patterns; DCs, Dendritic Cells; DEGs, Differentially Expressed Genes; ECM, Extracellular Matrix; ELISA, Enzyme-Linked Immunosorbent Assay; ER, Estrogen Receptor; EVs, Extracellular Vesicles; GO, Gene Ontology; H&E, Hematoxylin and eosin; HER2, Human epidermal growth factor receptor 2; IL-17, Interleukin-17; IC50, Half Maximal Inhibitory Concentration; ICD, Immunogenic Cell Death; IHC, Immunohistochemistry; IR-780, Indocyanine Green Analog 780; KEGG, Kyoto Encyclopedia of Genes and Genomes; Ki-67, Proliferation Marker Protein Ki-67; MDSCs, Myeloid-Derived Suppressor Cells; MEVs, Macrophage-derived

Extracellular Vesicles; PR, Progesterone Receptor; PTX, Paclitaxel; REVs, Erythrocyte-derived Extracellular Vesicles; ROS, Reactive Oxygen Species; TCA, Tricarboxylic Acid Cycle; TIME, Tumor Immune Microenvironment; TAMs, Tumor-Associated Macrophages; Treg, Regulatory T Cell; TUNEL, Terminal deoxynucleotidyl transferase dUTP Nick End Labeling; TNBC, Triple-negative breast cancer; WB, Western blot.

Data Sharing Statement

All data needed to support the conclusions in the paper are presented in the paper and/or the Supplementary Material. Additional data related to this paper may be requested from the corresponding author (Weijie Zhang) upon request.

Ethics Statement

All animal experiment protocols using mice were approved by the Animal Ethics Committee of Nanjing First Hospital (Nanjing, China, DWSY-24136592).All animal procedures were carried out ethically and humanely.

Author Contributions

All authors made a significant contribution to the work reported, whether that is in the conception, study design, execution, acquisition of data, analysis and interpretation, or in all these areas; took part in drafting, revising or critically reviewing the article; gave final approval of the version to be published; have agreed on the journal to which the article has been submitted; and agree to be accountable for all aspects of the work.

Funding

This work was supported by the National Natural Science Foundation of China (82102917, 81672380), Nanjing Special Foundation for Health Science and Technology Development (ZKX23012, YKK23104), Crosswise Project of Nanjing University (2020-K001), Bethune Charitable Foundation project (Z04J2023E095) and State Key Laboratory of Advanced Drug Delivery and Release Systems (DSQZ-QN-20250106).

Disclosure

The authors report no conflicts of interest in this work.

References

1. Siegel RL, Kratzer TB, Giaquinto AN, Sung H, Jemal A. Cancer statistics, 2025. *CA-Cancer J Clin*. 2025;75(1):10–45. doi:10.3322/caac.21871
2. Filho AM, Laversanne M, Ferlay J, et al. The GLOBOCAN 2022 cancer estimates: data sources, methods, and a snapshot of the cancer burden worldwide. *Int J Cancer*. 2025;156(7):1336–1346. doi:10.1002/ijc.35278
3. Fu MX, Peng ZM, Wu M, Lv DP, Li YP, Lyu S. Current and future burden of breast cancer in Asia: a GLOBOCAN data analysis for 2022 and 2050. *Breast*. 2025;79. doi:10.1016/j.breast.2024.103835
4. Schiff PB, Fant J, Horwitz SB. Promotion of microtubule assembly in vitro by taxol. *Nature*. 1979;277(5698):665–667. doi:10.1038/277665a0
5. Schiff PB, Horwitz SB. TAXOL STABILIZES MICROTUBULES IN MOUSE FIBROBLAST CELLS. *Proc Natl Acad Sci USA Biol Sci*. 1980;77(3):1561–1565. doi:10.1073/pnas.77.3.1561
6. Assaraf YG, Brozovic A, Goncalves AC, et al. The multi-factorial nature of clinical multidrug resistance in cancer. *Drug Resist Update*. 2019:46. doi:10.1016/j.drup.2019.100645
7. Housman G, Byler S, Heerboth S, et al. Drug resistance in cancer: an overview. *Cancers*. 2014;6(3):1769–1792. doi:10.3390/cancers6031769
8. Wang X, Zhang H, Chen X. Drug resistance and combating drug resistance in cancer. *Cancer Drug Resist*. 2019;2(2):141–160. doi:10.20517/cdr.2019.10
9. Garrido-Castro AC, Lin NU, Polyak K. Insights into molecular classifications of triple-negative breast cancer: improving patient selection for treatment. *Cancer Discov*. 2019;9(2):176–198. doi:10.1158/2159-8290.Cd-18-1177
10. Schmid P, Abraham J, Chan S, et al. Capivasertib plus paclitaxel versus placebo plus paclitaxel as first-line therapy for metastatic triple-negative breast cancer: the PAKT Trial. *J Clin Oncol*. 2020;38(5):423–433. doi:10.1200/jco.19.00368
11. Kim B-E, Nevitt T, Thiele DJ. Mechanisms for copper acquisition, distribution and regulation. *Nat Chem Biol*. 2008;4(3):176–185. doi:10.1038/nchembio.72
12. Xue Q, Kang R, Klionsky DJ, Tang D, Liu J, Chen X. Copper metabolism in cell death and autophagy. *Autophagy*. 2023;19(8):2175–2195. doi:10.1080/15548627.2023.2200554
13. Kahlson MA, Dixon SJ. Copper-induced cell death. *Science*. 2022;375(6586):1231–1232. doi:10.1126/science.abo3959
14. Tsvetkov P, Coy S, Petrova B, et al. Copper induces cell death by targeting lipoylated TCA cycle proteins. *Science*. 2022;375(6586):1254. doi:10.1126/science.abf0529

15. Vasan K, Werner M, Chandel NS. Mitochondrial metabolism as a target for cancer therapy. *Cell Metab*. 2020;32(3):341–352. doi:10.1016/j.cmet.2020.06.019
16. Tsvetkov P, Detappe A, Cai K, et al. Mitochondrial metabolism promotes adaptation to proteotoxic stress. *Nat Chem Biol*. 2019;15(7):681. doi:10.1038/s41589-019-0291-9
17. Jiang Y, Huo Z, Qi X, Zuo T, Wu Z. Copper-induced tumor cell death mechanisms and antitumor theragnostic applications of copper complexes. *Nanomedicine*. 2022;17(5):303–324. doi:10.2217/nnm-2021-0374
18. Zhang Y, Ya S, Huang J, et al. Spatial isolation of single Copper(I) sites for cascade enzyme-like catalysis and simultaneous ferroptosis/cuproptosis boosted immunotherapy. *Exploration*. 2025:e20240275. doi:10.1002/EXP.20240275
19. Krysko DV, Garg AD, Kaczmarek A, Krysko O, Agostinis P, Vandenabeele P. Immunogenic cell death and DAMPs in cancer therapy. *Nat Rev Cancer*. 2012;12(12):860–875. doi:10.1038/nrc3380
20. Panaretakis T, Kepp O, Brockmeier U, et al. Mechanisms of pre-apoptotic calreticulin exposure in immunogenic cell death. *EMBO J*. 2009;28(5):578–590. doi:10.1038/emboj.2009.1
21. Obeid M, Tesniere A, Ghiringhelli F, et al. Calreticulin exposure dictates the immunogenicity of cancer cell death. *Nat Med*. 2007;13(1):54–61. doi:10.1038/nm1523
22. Yamazaki T, Hannani D, Poirier-Colame V, et al. Defective immunogenic cell death of HMGB1-deficient tumors: compensatory therapy with TLR4 agonists. *Cell Death Differ*. 2014;21(1):69–78. doi:10.1038/cdd.2013.72
23. A S-DV, Anel A, Naval J, Marzo I. Immunogenic cell death and immunotherapy of multiple myeloma. *Front Cell Dev Biol*. 2019;7. doi:10.3389/fcell.2019.00050
24. Wang N, Liu Y, Peng D, et al. Copper-based composites nanoparticles improve triple-negative breast cancer treatment with induction of apoptosis-cuproptosis and immune activation. *Adv Healthc Mater*. 2024;13(28):e2401646. doi:10.1002/adhm.202401646
25. Xu X, Li H, Tong B, et al. Biomimetic nano-regulator that induces cuproptosis and lactate-depletion mediated ROS storm for metalloimmunotherapy of clear cell renal cell carcinoma. *Adv Healthc Mater*. 2024;13(28):e2400204. doi:10.1002/adhm.202400204
26. He Y, Zhang S, She Y, et al. Innovative utilization of cell membrane-coated nanoparticles in precision cancer therapy. *Exploration*. 2024;4(6):20230164. doi:10.1002/EXP.20230164
27. Alvarez-Erviti L, Seow Y, Yin H, Betts C, Lakhal S, Wood MJA. Delivery of siRNA to the mouse brain by systemic injection of targeted exosomes. *Nat Biotechnol*. 2011;29(4):341–U179. doi:10.1038/nbt.1807
28. S-i O, Takanashi M, Sudo K, et al. Systemically injected exosomes targeted to EGFR deliver antitumor microRNA to breast cancer cells. *Mol Ther*. 2013;21(1):185–191. doi:10.1038/mt.2012.180
29. Tian Y, Li S, Song J, et al. A doxorubicin delivery platform using engineered natural membrane vesicle exosomes for targeted tumor therapy. *Biomaterials*. 2014;35(7):2383–2390. doi:10.1016/j.biomaterials.2013.11.083
30. Meldolesi J. Exosomes and ectosomes in intercellular communication. *Curr Biol*. 2018;28(8):R435–R444. doi:10.1016/j.cub.2018.01.059
31. Zhao Z, Zlokovic BV. Remote control of BBB: a tale of exosomes and microRNA. *Cell Res*. 2017;27(7):849–850. doi:10.1038/cr.2017.71
32. Lou K, Luo H, Jiang X, Feng S. Applications of emerging extracellular vesicles technologies in the treatment of inflammatory diseases. *Front Immunol*. 2024;15. doi:10.3389/fimmu.2024.1364401
33. Wang Y, Zhao M, Liu S, et al. Macrophage-derived extracellular vesicles: diverse mediators of pathology and therapeutics in multiple diseases. *Cell Death Dis*. 2020;11(10). doi:10.1038/s41419-020-03127-z
34. Chen QY, Gao B, Tong D, Huang C. Crosstalk between extracellular vesicles and tumor-associated macrophage in the tumor microenvironment. *Cancer Lett*. 2023;552. doi:10.1016/j.canlet.2022.215979
35. Haney MJ, Zhao Y, Jin YS, et al. Macrophage-derived extracellular vesicles as drug delivery systems for triple negative breast cancer (TNBC) therapy. *J Neuroimmune Pharm*. 2020;15(3):487–500. doi:10.1007/s11481-019-09884-9
36. Guo P, Huang J, Wang L, et al. ICAM-1 as a molecular target for triple negative breast cancer. *Proc Natl Acad Sci U S A*. 2014;111(41):14710–14715. doi:10.1073/pnas.1408556111
37. Yuan D, Zhao Y, Banks WA, et al. Macrophage exosomes as natural nanocarriers for protein delivery to inflamed brain. *Biomaterials*. 2017;142:1–12. doi:10.1016/j.biomaterials.2017.07.011
38. Kaur S, Singh SP, Elkahloun AG, Wu W, Abu-Asab MS, Roberts DD. CD47-dependent immunomodulatory and angiogenic activities of extracellular vesicles produced by T cells. *Matrix Biol*. 2014;37:49–59. doi:10.1016/j.matbio.2014.05.007
39. Long KB, Beatty GL. Harnessing the antitumor potential of macrophages for cancer immunotherapy. *OncoImmunology*. 2013;2(12). doi:10.4161/onci.26860
40. Wei Z, Zhang X, Yong T, et al. Boosting anti-PD-1 therapy with metformin-loaded macrophage-derived microparticles. *Nat Commun*. 2021;12(1). doi:10.1038/s41467-020-20723-x
41. Wu P, Zhang B, Ocansey DKW, Xu W, Qian H. Extracellular vesicles: a bright star of nanomedicine. *Biomaterials*. 2021;269. doi:10.1016/j.biomaterials.2020.120467
42. Saleh AF, Lazaro-Ibanez E, Forsgard MAM, et al. Extracellular vesicles induce minimal hepatotoxicity and immunogenicity. *Nanoscale*. 2019;11(14):6990–7001. doi:10.1039/c8nr08720b
43. Raposo G, Stoorvogel W. Extracellular vesicles: exosomes, microvesicles, and friends. *J Cell Biol*. 2013;200(4):373–383. doi:10.1083/jcb.201211138
44. Mathivanan S, Ji H, Simpson RJ. Exosomes: extracellular organelles important in intercellular communication. *J Proteomics*. 2010;73(10):1907–1920. doi:10.1016/j.jprot.2010.06.006
45. Jiang X-C, Gao J-Q. Exosomes as novel bio-carriers for gene and drug delivery. *Int J Pharm*. 2017;521(1–2):167–175. doi:10.1016/j.ijpharm.2017.02.038
46. Mulcahy LA, Pink RC, Carter DRF. Routes and mechanisms of extracellular vesicle uptake. *J Extracell Vesicles*. 2014;3. doi:10.3402/jev.v3.24641
47. Rouzier R, Rajan R, Wagner P, et al. Microtubule-associated protein tau: a marker of paclitaxel sensitivity in breast cancer. *Proc Natl Acad Sci U S A*. 2005;102(23):8315–8320. doi:10.1073/pnas.0408974102
48. Tang W, Wu J, Wang L, et al. Bioactive layered double hydroxides for synergistic sonodynamic/cuproptosis anticancer therapy with elicitation of the immune response. *ACS Nano*. 2024;18(15):10495–10508. doi:10.1021/acsnano.3c11818

49. Huang Q-X, Liang J-L, Chen Q-W, et al. Metal-organic framework nanoagent induces cuproptosis for effective immunotherapy of malignant glioblastoma. *Nano Today*. 2023:51. doi:10.1016/j.nantod.2023.101911
50. Lu X, Chen X, Lin C, et al. Elesclomol loaded copper oxide nanoplatform triggers cuproptosis to enhance antitumor immunotherapy. *Adv Sci*. 2024;11(18). doi:10.1002/advs.202309984
51. Liu Y, Niu R, Zhao H, et al. Single-Site nanozymes with a highly conjugated coordination structure for antitumor immunotherapy via cuproptosis and cascade-enhanced T lymphocyte activity. *J Am Chem Soc*. 2024;146(6):3675–3688. doi:10.1021/jacs.3c08622
52. Hu F, Huang J, Bing T, et al. Stimulus-responsive copper complex nanoparticles induce cuproptosis for augmented cancer immunotherapy. *Adv Sci*. 2024;11(13). doi:10.1002/advs.202309388
53. Ianevski A, Giri AK, Aittokallio T. SynergyFinder 2.0: visual analytics of multi-drug combination synergies. *Nucleic Acids Res*. 2020;48(W1): W488–W493. doi:10.1093/nar/gkaa216
54. Ianevski A, Giri AK, Aittokallio T. SynergyFinder 3.0: an interactive analysis and consensus interpretation of multi-drug synergies across multiple samples. *Nucleic Acids Res*. 2022;50(W1):W739–W743. doi:10.1093/nar/gkac382
55. Ianevski A, He L, Aittokallio T, Tang J. SynergyFinder: a web application for analyzing drug combination dose-response matrix data. *Bioinformatics*. 2017;33(15):2413–2415. doi:10.1093/bioinformatics/btx162
56. Korn T, Bettelli E, Oukka M, Kuchroo VK. IL-17 and Th17 cells. *Annu Rev Immunol*. 2009;27:485–517. doi:10.1146/annurev.immunol.021908.132710
57. Gaffen SL, Jain R, Garg AV, Cua DJ. The IL-23-IL-17 immune axis: from mechanisms to therapeutic testing. *Nat Rev Immunol*. 2014;14 (9):585–600. doi:10.1038/nri3707
58. Conti HR, Shen F, Nayyar N, et al. Th17 cells and IL-17 receptor signaling are essential for mucosal host defense against oral candidiasis. *J Exp Med*. 2009;206(2):299–311. doi:10.1084/jem.20081463
59. Ishigame H, Kakuta S, Nagai T, et al. Differential roles of Interleukin-17A and-17F in host defense against mucoepithelial bacterial infection and allergic responses. *Immunity*. 2009;30(1):108–119. doi:10.1016/j.immuni.2008.11.009
60. Kryczek I, Banerjee M, Cheng P, et al. Phenotype, distribution, generation, and functional and clinical relevance of Th17 cells in the human tumor environments. *Blood*. 2009;114(6):1141–1149. doi:10.1182/blood-2009-03-208249
61. Green DR, Llambi F. Cell death signaling. *Cold Spring Harbor Perspect Biol*. 2015;7(12). doi:10.1101/cshperspect.a006080
62. Ruvolo PP, Deng X, May WS. Phosphorylation of Bcl2 and regulation of apoptosis. *LEUKEMIA*. 2001;15(4):515–522. doi:10.1038/sj.leu.2402090
63. Hata AN, Engelman JA, Faber AC. The BCL2 family: key mediators of the apoptotic response to targeted anticancer therapeutics. *Cancer Discov*. 2015;5(5):475–487. doi:10.1158/2159-8290.CD-15-0011
64. Sung H, Ferlay J, Siegel RL, et al. Global cancer statistics 2020: GLOBOCAN estimates of incidence and mortality worldwide for 36 cancers in 185 countries. *CA-Cancer J Clin*. 2021;71(3):209–249. doi:10.3322/caac.21660
65. Gao X, Huang H, Pan C, et al. Disulfiram/Copper induces immunogenic cell death and enhances CD47 blockade in hepatocellular carcinoma. *Cancers*. 2022;14(19). doi:10.3390/cancers14194715
66. Guo Y, Fan Y, Wang Z, et al. Chemotherapy mediated by biomimetic polymeric nanoparticles potentiates enhanced tumor immunotherapy via amplification of endoplasmic reticulum stress and mitochondrial dysfunction. *Adv Mater*. 2022;34(47). doi:10.1002/adma.202206861
67. Yan X, Chen C, Ren Y, et al. A dual-pathway pyroptosis inducer based on Au-Cu(2-x)Se@ZIF-8 enhances tumor immunotherapy by disrupting the zinc ion homeostasis. *Acta Biomater*. 2024;188:329–343. doi:10.1016/j.actbio.2024.09.015
68. Chen M, Wang D, Fan L, et al. The copper (II) complex of salicylate phenanthroline induces immunogenic cell death of colorectal cancer cells through inducing endoplasmic reticulum stress. *Int Immunopharmacol*. 2024;132:111980. doi:10.1016/j.intimp.2024.111980
69. Yao L, Zhu X, Shan Y, Zhang L, Yao J, Xiong H. Recent progress in anti-tumor nanodrugs based on tumor microenvironment redox regulation. *Small*. 2024;20(25):e2310018. doi:10.1002/smll.202310018
70. Nie X, Wang Y, Zhao H, Guo M, Liu Y, Xing M. As(3+) or/and Cu(2+) exposure triggers oxidative stress imbalance, induces inflammatory response and apoptosis in chicken brain. *Ecotoxicol Environ Saf*. 2020;203:110993. doi:10.1016/j.ecoenv.2020.110993
71. Kim YJ, Bond GJ, Tsang T, Posimo JM, Busino L, Brady DC. Copper chaperone ATOX1 is required for MAPK signaling and growth in BRAF mutation-positive melanoma. *Metallomics*. 2019;11(8):1430–1440. doi:10.1039/c9mt00042a
72. Xie J, Shao Z, Li C, Zeng C, Xu B. Cuproptosis-related gene ATOX1 promotes MAPK signaling and diffuse large B-cell lymphoma proliferation via modulating copper transport. *Biomol Biomed*. 2024;25(1):16–28. doi:10.17305/bb.2024.10536